

HOMOGENIZATION-BASED MIXED MULTISCALE FINITE ELEMENTS FOR PROBLEMS WITH ANISOTROPY*

TODD ARBOGAST†

Abstract. Multiscale finite element numerical methods are used to solve flow problems when the coefficient in the elliptic operator is heterogeneous. A popular mixed multiscale finite element has basis functions which can be defined only over pairs of elements, so we call it a “dual-support” element. We show by example that it can fail to reproduce constant flow fields, and so fails to converge in any meaningful way. The problem arises when the coefficient is an anisotropic tensor. A new approach to multiscale finite elements based on the microscale structure theory of homogenization is presented to avoid the problems with anisotropy. Five numerical test cases are presented to evaluate and contrast the methods. The first involves anisotropy, and the second is similar in that, although it has an isotropic coefficient, its heterogeneity leads to an anisotropic homogenized coefficient. As expected, the popular method has difficulty—while the new method shows no difficulty—with either anisotropy or macroscale implied anisotropy. The final three tests involve heterogeneous and channelized cases, and features of the new method are shown to be important for good approximation. Finally, for a two-scale coefficient, a proof of convergence is presented for standard mixed multiscale finite elements that reduces to four simple steps. From its simplicity, one can easily see that the popular elements fail only the step related to the counterexample, and we conjecture, but do not prove, that the new homogenization-based elements converge.

Key words. elliptic, heterogeneous, mixed method, convergence, dual-support elements, dual-element support

AMS subject classifications. 65N15, 65N30, 35J20

DOI. 10.1137/100788677

1. Introduction. To illustrate ideas, we consider only the following simple second order elliptic equation, which in mixed form is

$$(1.1) \quad \mathbf{u} = -a_\epsilon \nabla p \quad \text{in } \Omega,$$

$$(1.2) \quad \nabla \cdot \mathbf{u} = f \quad \text{in } \Omega,$$

$$(1.3) \quad \mathbf{u} \cdot \nu = 0 \quad \text{on } \partial\Omega,$$

where $\Omega \subset \mathbb{R}^d$, $d = 2, 3$, is the problem domain, ν is the outer unit normal, $a_\epsilon(x)$ is a tensor, uniformly positive definite, $f(x)$ is the source or sink term, and the unknowns are *pressure* $p(x)$ and *velocity* $\mathbf{u}(x)$. The difficulty arises from the coefficient a_ϵ , which is assumed to be highly heterogeneous; that is, a_ϵ varies on a fine scale $\epsilon \ll 1$. Resolution of the solution requires that it be approximated on a mesh \mathcal{T}_h of maximal spacing $h < \epsilon$; however, this is often not computationally feasible. To reduce the computational workload, and to increase parallelism, various multiscale approximation schemes have been proposed, including multiscale finite element and finite volume methods [22], [2], [27], [28], [23], [33], [34], [18], [1], [3], variational multiscale methods and related subgrid up-scaling and component mode synthesis techniques [29], [30], [9], [4], [8], [5], [6], [31], [7], [36], [38], [39], [25], generalized finite elements and partition of unity methods [13], [11],

*Received by the editors March 15, 2010; accepted for publication (in revised form) March 4, 2011; published electronically June 27, 2011. This work was supported by the U.S. National Science Foundation under grants DMS-0408489 and DMS-0835745.

<http://www.siam.org/journals/mms/9-2/78867.html>

†Department of Mathematics, University of Texas, Austin, TX 78712 and Institute for Computational Engineering and Sciences, University of Texas, Austin, TX 78712 (arbogast@ices.utexas.edu).

[43], [12], the heterogeneous multiscale method [21], the multiscale mortar method [41], [10], multiscale solver methods [37], [24], [32], [40], and many others.

In this paper, in sections 2 and 6, we consider certain mixed multiscale finite element methods, which are also variational multiscale methods, since these types of methods have implicitly defined multiscale finite elements [7]. In a sense to be made clear, the multiscale elements we consider are based on the standard, nonmultiscale mixed elements of first order due to Raviart and Thomas (RT0) [42] and of second order due to Brezzi, Douglas, and Marini (BDM1) [16], [15]. The standard mixed multiscale elements of first order are implicit in the work of Arbogast, Minkoff, and Keenan and later defined by Chen and Hou (ME0) [9], [18], and the ones of second order are due to Arbogast (ME1) [4], [5], [7]. We also consider the simplest variant of the “dual-support” element defined by Aarnes, Krogstad, and Lie (MD) [1], [3]. In section 3, we show that this element cannot converge as the mesh size tends to zero by constructing a family of counterexamples. The problem arises when a_ϵ is an anisotropic tensor.

We define a new “homogenization-based” mixed multiscale finite element HE0 in section 5 that uses some of the ideas of the MD element, but does not (apparently) have the same problem with anisotropy. Homogenization theory, section 4, suggests that microscale variation in \mathbf{u} can be represented to order $\mathcal{O}(\sqrt{\epsilon})$ as a fixed function \mathcal{A}_ϵ depending on ϵ times the smooth homogenized solution \mathbf{u}_0 . We therefore base our new finite element on an explicit representation of \mathcal{A}_ϵ and on an approximation of \mathbf{u}_0 , in our case, by a constant vector. We also note a variant HE0-OS that uses oversampling to define \mathcal{A}_ϵ .

In section 7, we present a series of five test cases to evaluate and contrast the methods. Generally, HE0-OS performs best. The first test case uses a constant but anisotropic a_ϵ . The second test case uses a locally isotropic a_ϵ that has streaks of alternating high and low values. Under homogenization, this streaked a_ϵ tends to the first case. These two cases show the problems that MD can experience for anisotropic problems, both directly and also as a macroscopic effect under upscaling, and also shows no such difficulty for HE0. The third test case is moderately heterogeneous, and all methods work relatively well. The final two test cases involve channelized flows.

A complete summary of our results and conclusions is given in section 8.

Theoretical convergence results are presented in the appendix for ME0 and ME1. The results are not new, but the proof reduces to four simple steps. The MD elements fail only one step, which is related to our counterexample. We do not extend the proof to HE0 elements because of technical issues related to homogenization theory, but the simplicity of the proof does allow us to conjecture that HE0 should work well, as our numerical results show.

To fix some of our notation, for $\omega \subset \Omega$, let $\|\cdot\|_{k,p,\omega}$ denote the norm of the Sobolev space $W^{k,p}(\omega)$ of k times differentiable functions in $L^p(\omega)$, $1 \leq p \leq \infty$. Similarly, $\|\cdot\|_{k,\omega}$ is the norm of the Hilbert space $H^k(\omega) = W^{k,2}(\omega)$. We may omit ω in the notation if it is Ω .

2. Some mixed multiscale finite element methods. For most of the discussion, it suffices that $\Omega \subset \mathbb{R}^d$, $d = 2, 3$, is polygonal and that \mathcal{T}_H is a conforming mesh of simplices or rectangles of maximal element diameter $H > 0$. However, for a few critical results, we require a mesh of rectangles, so we tacitly assume this for the rest of the paper. Between two adjacent elements, we denote by e the $(d - 1)$ -dimensional intersection, referred to as an “edge” (we use the two-dimensional terminology— e is a face in three dimensions). Let the set of edges be denoted \mathcal{E}_H .

At times we will need a consistent normal direction, so for $e \in \mathcal{E}_H$, let ν_e denote a fixed unit normal vector. Moreover, if $e \not\subset \partial\Omega$, let $E_{e,1}$ and $E_{e,2}$ be the two elements that

share edge e , where ν_e points from $E_{e,1}$ to $E_{e,2}$. If $e \subset \partial\Omega$, simply let $\nu_e = \nu$, $E_{e,1}$ be the element containing e , and $E_{e,2}$ be empty. Finally, let the dual-element support domain be $E_e = E_{e,1} \cup E_{e,2} \cup e$.

Let $\mathbf{V} = H(\text{div}; \Omega) = \{\mathbf{v} \in (L^2(\Omega))^d: \nabla \cdot \mathbf{v} \in L^2(\Omega)\}$ and $W = L^2(\Omega)/\mathbb{R}$. Then the standard variational problem for (1.1)–(1.3) is to find $(\mathbf{u}, p) \in \mathbf{V} \times W$ such that

$$(2.1) \quad (\alpha_\epsilon \mathbf{u}, \mathbf{v}) - (p, \nabla \cdot \mathbf{v}) = 0 \quad \forall \mathbf{v} \in \mathbf{V},$$

$$(2.2) \quad (\nabla \cdot \mathbf{u}, w) = (f, w) \quad \forall w \in W,$$

where $\alpha_\epsilon = a_{\epsilon^{-1}}$ and (\cdot, \cdot) is the $L^2(\Omega)$ innerproduct.

Once conforming finite element spaces $\mathbf{V}_H \times W_H \subset \mathbf{V} \times W$ are defined, the standard mixed finite element method is to find $(\mathbf{u}_H, p_H) \in \mathbf{V}_H \times W_H$ such that

$$(2.3) \quad (\alpha_\epsilon \mathbf{u}_H, \mathbf{v}) - (p_H, \nabla \cdot \mathbf{v}) = 0 \quad \forall \mathbf{v} \in \mathbf{V}_H,$$

$$(2.4) \quad (\nabla \cdot \mathbf{u}_H, w) = (f, w) \quad \forall w \in W_H.$$

If we use special ϵ -scale-dependent finite elements, we call this a mixed multiscale finite element method.

The lowest order mixed finite elements that we consider all take W_H as the set of piecewise constants; that is,

$$(2.5) \quad W_H = \{w \in W: w|_E \text{ is constant } \forall E \in \mathcal{T}_H\}.$$

2.1. Raviart-Thomas (RT0) elements. The standard lowest order RT0 mixed finite elements [42], [17] are defined on a rectangular element E so that $\mathbf{V}^{\text{RT0}}(E)$ is a vector for which the i th component is linear in x_i and constant in the other variables. These are pieced together so that

$$\mathbf{V}_H^{\text{RT0}} = \{\mathbf{v} \in \mathbf{V}: \mathbf{v}|_E \in \mathbf{V}^{\text{RT0}}(E) \forall E \in \mathcal{T}_H\};$$

that is, the normal component of velocity is continuous across all edges.

2.1.1. Element definition. A basis can be found by defining degrees of freedom as the normal fluxes on each element edge. This vector basis can be constructed by solving boundary value problems on each element E . For each edge $e \subset \partial E$, the vector $\mathbf{v}_e^{\text{RT0}}$ and unused scalar ϕ_e^{RT0} are the solution of the mixed problem

$$(2.6) \quad \mathbf{v}_e^{\text{RT0}} = -\nabla \phi_e^{\text{RT0}} \quad \text{in } E,$$

$$(2.7) \quad \nabla \cdot \mathbf{v}_e^{\text{RT0}} = \nu_E \cdot \nu_e |e|/|E| \quad \text{in } E,$$

$$(2.8) \quad \mathbf{v}_e^{\text{RT0}} \cdot \nu_E = \begin{cases} 0 & \text{on } \partial E \setminus e, \\ 1 & \text{on } e, \end{cases}$$

where ν_E is the outward normal to ∂E . Given $e \in \mathcal{E}_H$, we solve the problem above on both $E_{e,1}$ and $E_{e,2}$, which piece together to give $\mathbf{v}_e^{\text{RT0}} \in \mathbf{V}$.

2.1.2. Dual-element support definition. Alternatively, when \mathcal{T}_H is rectangular, a basis can be constructed on the dual-support domain E_e . For each edge $e \in \mathcal{E}_H$, solve

$$(2.9) \quad \mathbf{v}_e^{\text{RT0}} = -\nabla\phi_e^{\text{RT0}} \quad \text{in } E_e,$$

$$(2.10) \quad \nabla \cdot \mathbf{v}_e^{\text{RT0}} = \nu_{E_{e,i}} \cdot \nu_e |e|/|E_{e,i}| \quad \text{in } E_{e,i}, \quad i = 1, 2,$$

$$(2.11) \quad \mathbf{v}_e^{\text{RT0}} \cdot \nu = 0 \quad \text{on } \partial E_e.$$

The equivalence of definitions is not difficult to verify on rectangular grids, since the solution is piecewise linear in the flow direction and constant in the normal direction. However, this equivalence does *not* hold on triangles/simplices. Nevertheless, (2.9)–(2.11) suggest a multiscale element on general computational meshes (see section 2.3 below).

These elements have no dependence on the scale ϵ . It is well known (see, e.g., [42], [17], and also the appendix below) that

$$(2.12) \quad \|\mathbf{u} - \mathbf{u}_H^{\text{RT0}}\|_0 \leq C\|\mathbf{u}\|_1 H, \quad \|\nabla \cdot (\mathbf{u} - \mathbf{u}_H^{\text{RT0}})\|_0 \leq C\|f\|_1 H,$$

where C is independent of ϵ . However, $\|\mathbf{u}\|_1 = \mathcal{O}(\epsilon^{-1})$, so the method is useful only when $H < \epsilon$ [13], [27], i.e., when H resolves the fine-scale heterogeneity.

2.2. Variational multiscale elements (ME0) based on RT0. The variational multiscale method was first defined by Hughes et al. [29], [30] for the nonmixed problem, and for the mixed case by Arbogast, Minkoff, and Keenan [9], [4], [5]. It can be viewed (see [7]) as a variational framework that uses mixed multiscale finite elements, but also improves approximation of the fixed source term f in (1.2). For simplicity of exposition, we will omit this last modification until the numerical results in section 7 and consider only the effects of the multiscale finite elements.

The first and lowest order mixed multiscale finite element space $\mathbf{V}_H^{\text{ME0}}$ was defined implicitly in [9], [7] as a modification of the RT0 elements, and also later in [18]. A basis for the multiscale elements (RT0 ME0) can be realized by solving on each element E , for each edge $e \subset \partial E$,

$$(2.13) \quad \mathbf{v}_e^{\text{ME0}} = -a_\epsilon \nabla \phi_e^{\text{ME0}} \quad \text{in } E,$$

$$(2.14) \quad \nabla \cdot \mathbf{v}_e^{\text{ME0}} = \nu_E \cdot \nu_e |e|/|E| \quad \text{in } E,$$

$$(2.15) \quad \mathbf{v}_e^{\text{ME0}} \cdot \nu = \begin{cases} 0 & \text{on } \partial E \setminus e, \\ 1 & \text{on } e. \end{cases}$$

The normal trace along the interelement edge e is constant as for RT0 elements, but now $\mathbf{v}_e^{\text{ME0}}$ picks up some of the microstructure within E .

It is known that this method converges. From [6] we have a convergence estimate when $H < \epsilon$,

$$(2.16) \quad \|\mathbf{u} - \mathbf{u}_H^{\text{ME0}}\|_0 \leq C\|\mathbf{u}\|_1 H, \quad \|\nabla \cdot (\mathbf{u} - \mathbf{u}_H^{\text{ME0}})\|_0 \leq C\|f\|_1 H,$$

and, for $\epsilon < H$, from [18], [7] (see also the appendix below) the multiscale error estimate

$$(2.17) \quad \|\mathbf{u} - \mathbf{u}_H^{\text{ME0}}\|_0 \leq C\{H\|\mathbf{u}_0\|_1 + |\epsilon|\|\mathbf{u}_0\|_0 + \sqrt{\epsilon/H}\|\mathbf{u}_0\|_{0,\infty}\},$$

where \mathbf{u}_0 is a smooth function independent of ϵ and defined below in section 4 (where also condition (4.1) is made on the multiscale form of a_ϵ).

2.3. Multiscale dual-support (MD) elements. The MD finite elements that we consider were first used by Aarnes, Krogstad, and Lie [1], [3]. We consider only the simplest family of such finite elements. A basis for \mathbf{V}_H^{MD} can be constructed for each edge $e \in \mathcal{E}_H$ by solving on all of E_e

$$(2.18) \quad V_e^{\text{MD}} = -a_e \nabla \phi_e^{\text{MD}} \quad \text{in } E_e,$$

$$(2.19) \quad \nabla \cdot \mathbf{v}_e^{\text{MD}} = \nu_{E_{e,i}} \cdot \nu_e |e| / |E_{e,i}| \quad \text{in } E_{e,i}, \quad i = 1, 2,$$

$$(2.20) \quad v_e^{\text{MD}} \cdot \nu = 0 \quad \text{on } E_e.$$

We call this a *dual-support* finite element because it cannot be constructed by joining together pieces defined on each element $E \subset E_e$. That is, the shape on $E_{e,1}$ depends on $E_{e,2}$, and vice versa. Because of this fact, this is not actually a finite element in the classical sense of Ciarlet [20], although we will consider it so in this work.

When \mathcal{T}_H is rectangular and a_e is a constant diagonal tensor, these elements coincide with the RT0 elements (recall (2.9)–(2.11)). The normal trace along the interelement edge e is no longer constant, but there still is an average unit flux. The basis finite elements mimic a “typical” but local flow problem, so naturally one would think that they can better approximate flows in a global problem. However, we show in the next section that in fact this method fails to converge when the coefficient a_e is anisotropic. In fact, the counterexample uses a *constant* tensor, so nonconvergence is unrelated to the fine-scale heterogeneity.

3. Anisotropic counterexamples to convergence of MD. We give a family of examples where the MD elements fail to converge. For simplicity, consider the problem (1.1)–(1.3) on a square domain Ω , and use a uniform rectangular grid \mathcal{T}_H . The key is to take a constant tensor coefficient $a = a_e$ such that $a = Q^T \Lambda Q$, where Q is a rotation and Λ is a diagonal tensor. Assuming the grid aligns with the coordinate axes, we take a Λ that is not a scalar multiple of the identity, and a rotation Q that is not a multiple of $\pi/2$, so a genuine anisotropy is induced into the numerical problem.

It is a fact that, in this case, all of the MD basis functions \mathbf{v}_e^{MD} have a nonconstant normal trace on interelement edges $e \in \mathcal{E}_H$. That is, the MD basis functions become “twisted” in some sense, as shown in Figure 3.1. The problem is now manifest: the space \mathbf{V}_H^{MD} cannot reproduce constants, and so the method cannot converge in any reasonable sense.

Because a is constant, the same shape \mathbf{v}_e^{MD} is used everywhere in the grid (up to a rescaling). Indeed, the same shape is used for every H as well. As noted above, because there is anisotropy and it is not aligned with the grid, the shape \mathbf{v}_e^{MD} has a nonconstant trace along edges. For a general problem (with possibly nonconstant \mathbf{u}), as we shrink the

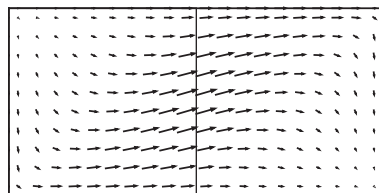


FIG. 3.1. The velocity basis function \mathbf{v}_e^{MD} for a constant, anisotropic coefficient a_e . The preferential direction is 30 degrees above the horizontal and 100 times the orthogonal direction. The nonconstant nature of the normal trace along the interelement edge e is very noticeable.

grid size H , the velocity \mathbf{u} has a nearly constant normal trace along edges because it is smooth. This difference between the shape and the velocity on the edges accounts for the nonconvergence.

There is nothing particularly special about the uniform rectangular grid. What is important is that there is at least one edge of (most) every element that is not aligned with one of the principal axes of a . In that case, the shape functions \mathbf{v}_e^{MD} have a non-constant normal trace on the edge e , and the same ideas as above apply. This counterexample also suggests that some dual-support elements may not work well in practice, or at the least that they must be used with care. We will define a convergent element that uses the dual-element support idea below in section 5.

This example is also a reasonable proxy for more complicated examples of coefficient fields a_ϵ , because directional preferences in the subfield effectively act as a tensor at the coarse scale, as homogenization theory and upscaling schemes verify. We show such a numerical example below in section 7.2.

4. Microscale structure from homogenization theory. At times we will denote the true solution to the problem (1.1)–(1.3), or, equivalently, (2.1)–(2.2), by $(\mathbf{u}_\epsilon, p_\epsilon)$, to emphasize its scale dependence.

We assume that the heterogeneity in the coefficient a in (1.1) has a separation of scales and therefore a regular form; specifically, we assume that

$$(4.1) \quad a_\epsilon(x) = a(x, x/\epsilon),$$

where $a(x, y)$ is periodic in y in the unit cube $Y = [0, 1]^d$. It is well established (see, e.g., [44], [14], [35], [26], [27], [7]) that $(\mathbf{u}_\epsilon, p_\epsilon)$ converges to the solution (\mathbf{u}_0, p_0) of the homogenized problem

$$(4.2) \quad \mathbf{u}_0 = -a_0 \nabla p_0 \quad \text{in } \Omega,$$

$$(4.3) \quad \nabla \cdot \mathbf{u}_0 = f \quad \text{in } \Omega,$$

$$(4.4) \quad \mathbf{u}_0 \cdot \nu = 0 \quad \text{on } \partial\Omega.$$

Here, the homogenized tensor coefficient $a_0(x)$ is given by

$$(4.5) \quad a_{0,ij}(x) = \int_Y a(x, y) \left(\delta_{ij} + \frac{\partial \omega_j(x, y)}{\partial y_i} \right) dy,$$

where $\omega_j(x, y)$, for each fixed $x \in \Omega$, is the y -periodic solution of the cell problem

$$(4.6) \quad -\nabla_y \cdot [a(x, y)(\nabla_y \omega_j(x, y) + \mathbf{e}_j)] = 0$$

with $\mathbf{e}_j \in \mathbb{R}^d$ being the j th standard unit vector.

The convergence result we need is given in [7, Theorem 5.2]. We state it below, with a result giving the microscale structure extracted carefully from an examination of the proof given there.

THEOREM 4.1. *Assume that (4.1) holds and $p_0 \in H^2(\Omega) \cap W^{1,\infty}(\Omega)$. Let $\alpha_0 = a_0^{-1}$ and define the fixed tensor*

$$(4.7) \quad \mathcal{A}_{ij}(x, y) = \sum_{k,\ell} a_{ik}(x, y) \left(\delta_{k\ell} + \frac{\partial \omega_\ell(x, y)}{\partial y_k} \right) \alpha_{0,\ell j},$$

which depends on $a(x, y)$, but not on the domain Ω . Then with $\mathcal{A}_\epsilon(x) = \mathcal{A}(x, x/\epsilon)$,

$$(4.8) \quad \mathbf{u}_\epsilon(x) = \mathcal{A}_\epsilon(x)\mathbf{u}_0(x) + \theta_\epsilon^\Omega(x),$$

where

$$(4.9) \quad \|\theta_\epsilon^\Omega\|_0 \leq C\{\epsilon\|\mathbf{u}_0\|_1 + \sqrt{\epsilon|\partial\Omega|}\|\mathbf{u}_0\|_{0,\infty}\}.$$

5. New homogenization-based elements (HE0 and HE0-OS). The structure result (4.8) shows that \mathbf{u} has ϵ -scale structure due to the heterogeneity in a very specific way, at least in the two-scale separation case of (4.1). Up to $\mathcal{O}(\sqrt{\epsilon})$, \mathbf{u} is an operator of a smooth function \mathbf{u}_0 : $\mathbf{u}_\epsilon \approx \mathcal{A}_\epsilon\mathbf{u}_0$. This suggests that the finite element space should consist of functions of the form

$$\{\mathcal{A}_\epsilon\mathbf{v}; \mathbf{v} \text{ is some nice smooth function}\}.$$

However, since in general \mathcal{A}_ϵ is a tensor, this definition would create finite element functions that lie outside $H(\text{div}; \Omega)$; that is, nonconforming finite elements. Moreover, the divergence $\nabla \cdot \mathcal{A}_\epsilon\mathbf{v}$ is not piecewise constant, making it difficult to verify the inf-sup condition [17], and in fact \mathcal{A}_ϵ need not be positive definite at each point. To avoid these difficulties, we modify the definition to enforce appropriate local boundary conditions, divergence properties, and positivity.

We define a new mixed multiscale finite element using homogenization theory, particularly (4.8), as a heuristic guide. The elements are well defined independently of assumption (4.1). In d dimensions, we have d multiscale finite element basis functions per edge $e \in \mathcal{E}_H$.

Our definition has two main steps for each $e \in \mathcal{E}_H$. In the first step, we solve the periodic cell problem (4.6) for each $\omega_j(x, y)$, and define \mathcal{A}_ϵ from it according to (4.7). In the locally periodic case, this is well defined. However, in practice, we do not have the separation of scales hypothesis, so we resort to the dual-element support idea to define a local version of (4.1). That is, we take $E_e^* = E_e$ to be Y , the domain of the local cell problem. Thus, for each edge $e \in \mathcal{E}_H$ and $j = 1, \dots, d$, we define $\omega_{e,j}(x)$ as the periodic solution to

$$(5.1) \quad -\nabla \cdot [a_\epsilon(\nabla\omega_{e,j} + \mathbf{e}_j)] = 0 \quad \text{in } E_e^*.$$

As mentioned earlier, in this paper we assume that the fine scale is solved exactly. In practice, (5.1) is solved on the fine grid using, say, RT0 elements. In mixed form, we solve

$$\begin{aligned} \psi_{e,j} &= -a_\epsilon(\nabla\omega_{e,j} + \mathbf{e}_j) \quad \text{in } E_e^*, \\ \nabla \cdot \psi_{e,j} &= 0 \quad \text{in } E_e^* \end{aligned}$$

with periodic boundary conditions on $\omega_{e,j}$ and $\psi_{e,j}$; that is, we solve for $(\psi_{e,j}, \omega_{e,j}) \in \mathbf{V}^* \times W^*$ such that

$$\begin{aligned} (\alpha_\epsilon \psi_{e,j}, \mathbf{v}) - (\omega_{e,j}, \nabla \cdot \mathbf{v}) &= -(\mathbf{e}_j, \mathbf{v}) \quad \forall \mathbf{v} \in \mathbf{V}^*, \\ (\nabla \cdot \psi_{e,j}, w) &= 0 \quad \forall w \in W^*, \end{aligned}$$

where $\mathbf{V}^* \times W^*$ is the RT0 space on E_e^* with periodic boundary conditions on \mathbf{V}^* . We can now define Ψ_e to be the matrix with columns $\psi_{e,j}$ and then (4.5) becomes

$$a_0^e = \frac{1}{|E_e^*|} \int_{E_e^*} \Psi_e(x) dx,$$

where $|E_e^*|$ is the measure of the set, and the tensor (4.7) near edge e is

$$(5.2) \quad \mathcal{A}_e(x) = \Psi_e(x) \alpha_0^e,$$

where, as usual, $\alpha_0^e = (a_0^e)^{-1}$.

In fact, we use only normal traces on e . Since u_0 is smooth, we approximate it by a polynomial, in our case, of degree zero. For example, on e in $d = 2$ dimensions, for constants c_1 and c_2 ,

$$\mathbf{u}_e \cdot \nu \approx \mathcal{A}_e \mathbf{u}_0 \cdot \nu \approx \mathcal{A}_e \begin{pmatrix} c_1 \\ c_2 \end{pmatrix} \cdot \nu = c_1 \mathcal{A}_e \mathbf{e}_1 \cdot \nu + c_2 \mathcal{A}_e \mathbf{e}_2 \cdot \nu.$$

Only the traces $\mathcal{A}_e(x) \mathbf{e}_i \cdot \nu$, $i = 1, \dots, d$ for $x \in e$ are required. In principle, we could use a higher order approximation here, but then W_H would also need to be modified.

The second main step of the definition is to solve for a basis for our new space $\mathbf{V}_H^{\text{HE0}}$. For each $e \in \mathcal{E}_H$ and $i = 1, \dots, d$, on each element $E \in \mathcal{T}_H$ for which ∂E^e , define $\mathbf{v}_e^{\text{HE0},i}$ from the problem

$$(5.3) \quad \mathbf{v}_e^{\text{HE0},i} = -a_e \nabla \phi_e^{\text{HE0},i} \quad \text{in } E,$$

$$(5.4) \quad \nabla \cdot \mathbf{v}_e^{\text{HE0},i} \in \mathbb{R} \quad \text{in } E,$$

$$(5.5) \quad \mathbf{v}_e^{\text{HE0},i} \cdot \nu = \begin{cases} 0 & \text{on } \partial E \setminus e, \\ \mathcal{A}_e \mathbf{e}_i \cdot \nu & \text{on } e, \end{cases}$$

where the constant in \mathbb{R} is given by the compatibility condition. Note that our finite element space V_H^{HE0} has d times the number of degrees of freedom as the previous spaces. If $\mathcal{A}_e \mathbf{e}_i \cdot \nu$ should vanish, $\mathbf{v}_e^{\text{HE0},i} = 0$ and we should either remove this function from the basis, or perhaps replace it with a standard element such as $\mathbf{v}_e^{\text{RT0}}$ or one of the $\mathbf{v}_e^{\text{BDM1},i}$ elements from section 6 below.

We note that Hou and Wu proposed an oversampling technique [27] that reduces the resonance error. This technique was applied to define a nonconforming variant of ME0 [18], and it could be applied to any of the methods noted in this paper. In particular, we propose to use it in the definition of the homogenization functions ω_j in (5.1); that is, we solve this problem (5.1) on a domain E_e^* larger than E_e . In our numerical results, the oversampled version (HE0-OS) in two dimensions uses the six elements that surround edge e (or fewer, if we are near $\partial\Omega$).

6. The additional finite elements BDM1 and ME1. Before presenting our numerical results, we note the definitions of two additional finite elements to which we will compare. These finite elements have as many degrees of freedom as the HE0 elements (i.e., d per edge). The standard, nonmultiscale elements are due to Brezzi, Douglas, and Marini in two dimensions [16] and Brezzi et al. in three [15]. These elements will be denoted as BDM1, and they use W_H as defined (piecewise constants over the elements). The velocity space $\mathbf{V}_H^{\text{BDM1}}$ uses linear (two dimensions) or bilinear (three dimensions) variation in the normal velocity on each edge, extended by a low order polynomial over the element.

The multiscale variant of the BDM1 (or BDDF1) elements is due to Arbogast [4]. It is defined for each $e \in \mathcal{E}_H$ and $i = 1, \dots, 2^{d-1}$. On each element $E \in \mathcal{T}_H$ for which ∂E^e , we solve the problem

$$(6.1) \quad \mathbf{v}_e^{\text{ME1},i} = -a_\epsilon \nabla \phi_e^{\text{ME1},i} \quad \text{in } E,$$

$$(6.2) \quad \nabla \cdot \mathbf{v}_e^{\text{ME1},i} \in \mathbb{R} \quad \text{in } E,$$

$$(6.3) \quad \mathbf{v}_e^{\text{ME1},i} \cdot \nu = \begin{cases} 0 & \text{on } \partial E \setminus e, \\ L_i & \text{on } e, \end{cases}$$

where the constant in \mathbb{R} is determined by the compatibility condition and the L_i form a basis for the linears on e in two dimensions and the bilinears in three dimensions.

7. Numerical results. In this section we consider several test cases in two dimensions (i.e., $d = 2$) designed to illustrate the ideas and methods discussed in this paper. Our test cases are driven by application to flow in natural porous media, wherein f represents wells and a_ϵ is the *permeability* of the medium, which is indeed highly heterogeneous and generally anisotropic.

For these tests, we assume that the domain Ω is a rectangle and the permeability is given on a fixed, fine, uniformly rectangular mesh \mathcal{T}_h of rectangles of maximal spacing h . We solve for the multiscale finite element solution on the coarsened, uniformly rectangular mesh \mathcal{T}_H , so $h \leq \epsilon < H$. The multiscale finite element basis is computed using RT0 elements on the fine mesh \mathcal{T}_h over the coarse elements $E \in \mathcal{T}_H$ or over the dual-support elements E_e for $e \in \mathcal{E}_H$.

Wells tend to be highly localized objects, and therefore require multiscale treatment. Often, f is zero over most of the domain, and nonzero in only a few isolated fine-scale elements. Because of the way W_H is defined (see (2.5)), the multiscale method (2.3)–(2.4) sees only $\mathcal{P}_{W_H} f$, where \mathcal{P}_{W_H} is the L^2 -projection onto W_H . Therefore, the well is smeared evenly over the coarse element it lies within. To correct for this smearing, all of our upscaled results use the constant correction part of the affine closure operator described in [4], [5], [7]. That is, we define the mixed multiscale finite element solution to be

$$\mathbf{u}_H = \hat{\mathbf{u}}_H + \tilde{\mathbf{u}}_H,$$

where $\hat{\mathbf{u}}_H$ is the multiscale finite element solution given by (2.3)–(2.4). If f is nonzero on coarse element $E \in \mathcal{T}_H$, then we compute $\tilde{\mathbf{u}}_H$ on E as the fine mesh solution to

$$(7.1) \quad \tilde{\mathbf{u}}_H = -a_\epsilon \nabla \tilde{p}_H \quad \text{in } E,$$

$$(7.2) \quad \nabla \cdot \tilde{\mathbf{u}}_H = f - \mathcal{P}_{W_H} f \quad \text{in } E,$$

$$(7.3) \quad \tilde{\mathbf{u}}_H \cdot \nu_E = 0 \quad \text{on } \partial E.$$

Again, we solve this problem on the fine mesh \mathcal{T}_h using RT0.

We concentrate on the velocity approximation, which is generally the variable of interest. Moreover, the pressure tends to be better approximated than the velocity, since the velocity is proportional to the pressure gradient.

7.1. A constant, anisotropic permeability. We begin our computational tests by considering a simple constant but anisotropic permeability on the unit square $\Omega = (0, 1)^2$ with an injection well in the lower left corner and a production well of opposite

strength in the upper right corner. We take $a = Q^T \Lambda Q$, where the rotation is through an angle $\tan \theta = 1/2$ so $\theta = 26.565$ degrees and in fact

$$a = \begin{pmatrix} 80.798 & 39.404 \\ 39.404 & 21.692 \end{pmatrix} = \begin{pmatrix} \cos \theta & -\sin \theta \\ \sin \theta & \cos \theta \end{pmatrix} \begin{pmatrix} 100.5 & 0 \\ 0 & 1.990 \end{pmatrix} \begin{pmatrix} \cos \theta & \sin \theta \\ -\sin \theta & \cos \theta \end{pmatrix}.$$

In this case, $\omega_j = 0$ for each j , and so the method HE0 is the same as ME0, with half the basis functions having constant fluxes across coarse edges and the other half of the “basis functions” vanishing. We reset the extra basis functions to have linear flux variation, so HE0 becomes ME1 (and oversampling does not come into play).

This is actually a very difficult problem. As shown in Figure 7.1, fluid is injected mainly along the preferred flow direction, bleeds through the domain, and is extracted again through the preferred flow direction. In all figures, the color scale depicts the speed of the velocity, and the arrows show the direction (and speed) of flow.

There is no need for a fine mesh \mathcal{T}_h to define the permeability; nevertheless, a fine mesh is needed to adequately resolve the solution. We approximated the solution on uniformly square meshes for $1/h = 20, 40, 80$, and 160 . To avoid changing the problem when the grid changes, the wells cover the bottom left and upper right corner elements of the 20×20 grid, and cover multiple cells for the finer grids. The effect of the wells, being discontinuous, is difficult to approximate. Even though the solution is smooth away from wells and BDM1 is second order convergent, we did not see numerical convergence on a uniform grid until $1/h = 80$ or $1/h = 160$. We take the BDM1 solution on the 160×160 grid, Figure 7.1, as the reference solution and compare our upscaled results to this.

In Figure 7.2, we show the solution using the HE0 = ME1 and MD methods. These upscaled computations all use the fine 160×160 grid decomposed into a coarse grid and a subgrid within each coarse element. Therefore each upscaled result has sufficient resolution to match the fine BDM1 solution, and any error is due to the size of the coarse grid and the multiscale elements used. We use coarse grids of size $1/H = 10, 20$, and 40 , that is, grids of size $10 \times 10, 20 \times 20$, and 40×40 . In all these cases $1/h = 160$, but the subgrid meshes decrease as $16 \times 16, 8 \times 8$, and 4×4 , respectively.

We note that HE0 = ME1 does a nice job reproducing the solution. However, MD exhibits a fluctuation across the domain of period the same as the the size H of the coarse grid. This is due to the twist in the basis function as described in section 3.

In Table 7.1, we give the relative errors of the HE0 = ME1, MD, and ME0 methods with respect to the fine 160×160 BDM1 solution for the test cases depicted above, as

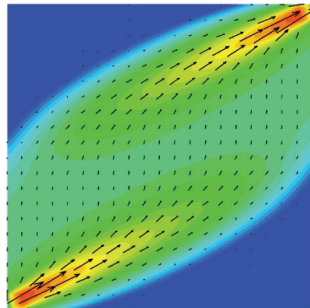


FIG. 7.1. Anisotropic test. The fine-scale BDM1 solution using a uniform 160×160 grid. The color depicts the speed, on a log scale from $4.6e-4$ to $4.6e-2$, and the arrows show the velocity direction (and speed).

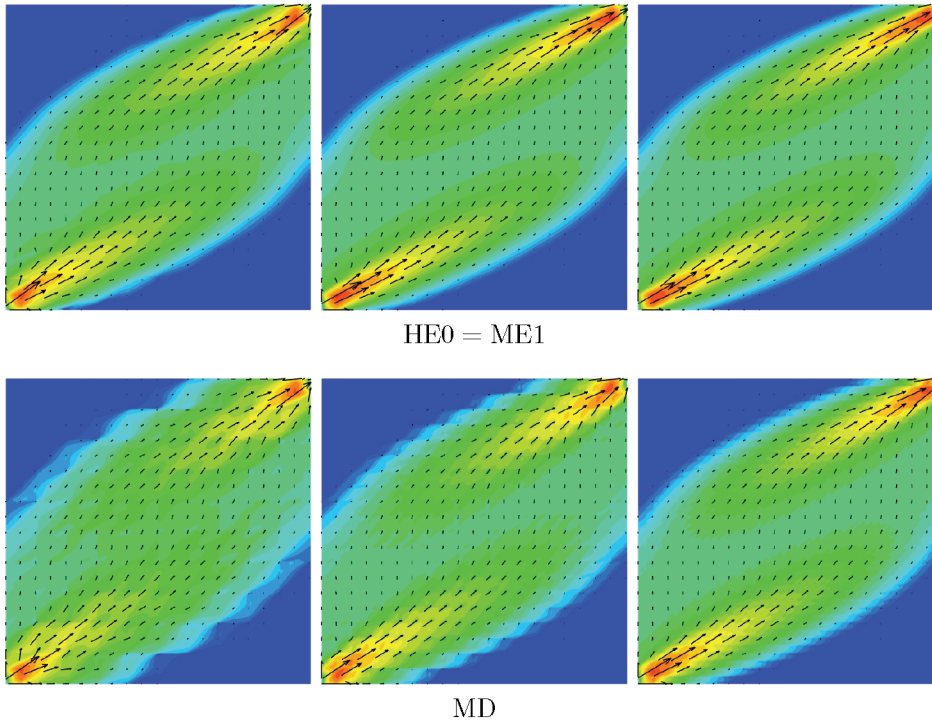


FIG. 7.2. Anisotropic test. The upscaled HE0 = ME1 (top) and MD (bottom) solution using fixed resolution $1/h = 160$ on coarse 10×10 , 20×20 , and 40×40 grids and 16×16 , 8×8 , and 4×4 subgrids, respectively, from left to right.

TABLE 7.1

Anisotropic test. Relative errors in the pressure and velocity for HE0 = ME1, MD, and ME0 relative to the 160×160 reference BDM1 solution. Both ℓ^2 and ℓ^∞ (maximum) norm errors are shown. Note that all computations work over the fine 160×160 grid. The number of coarse dof's depends on the number m of basis functions per edge.

Method	Coarse mesh $N \times N$	Subgrid mesh $n \times n$	Coarse dof's $2N(N-1)m$	Pressure error		Velocity error	
				ℓ^2	ℓ^∞	ℓ^2	ℓ^∞
HE0	10	16	360	0.0525	0.3152	0.2516	0.3427
	20	8	1520	0.0017	0.0188	0.0598	0.1919
	40	4	6240	0.0007	0.0069	0.0189	0.0460
	80	2	25280	0.0006	0.0055	0.0115	0.0155
MD	10	16	180	0.0551	0.2864	0.3709	0.3576
	20	8	760	0.0197	0.1388	0.2641	0.5451
	40	4	3120	0.0077	0.0603	0.1441	0.3565
	80	2	12640	0.0016	0.0143	0.0549	0.1335
	160	1	50880	0.0006	0.0055	0.0115	0.0155
ME0	10	16	180	0.0532	0.3098	0.3751	0.3864
	20	8	760	0.0171	0.1136	0.2513	0.4511
	40	4	3120	0.0052	0.0422	0.1241	0.2937
	80	2	12640	0.0016	0.0143	0.0549	0.1335
	160	1	50880	0.0006	0.0055	0.0115	0.0155

well as a few more to fill out the results. The observed convergence rate is difficult to assess, since we do not have a true analytic solution, but we can make some qualitative statements. We note first that the pressure is always rather well approximated in these tests. For the velocity, we note that MD and ME0 have similar errors, although perhaps the simpler ME0 is a bit better overall. If we were to plot the ME0 results as in Figure 7.2, we would see little difference between the two sets of figures. Finally, we note that the HE0 = ME1 method outperforms MD, but of course it uses twice as many degrees of freedom (dof's) on each edge. The total number of interface dof's are given, so one can see that HE0 = ME1 still outperforms MD by comparing the MD results with the HE0 = ME1 results for the next lower number of dof's in the table.

It was noted above that convergence should *not* be seen for MD because of the basis function twist effect. Nevertheless, it does appear that the solution is converging as $H \rightarrow 0$. This is due to at least two facts. First, the solution is difficult to approximate near the wells, where f is discontinuous, so there is error in these methods from the use of coarse grids. As we refine, we improve the approximation of the wells, and thereby reduce the error. This error appears to dominate the solution. Second, the subgrid is becoming coarser as we take $H \rightarrow 0$, so we lose the twisting effect of the basis functions as the subgrid is derefined, and paradoxically we reduce the twisting error.

The twisted basis function effect can be seen more clearly in Figure 7.3, where we fix the subgrid to 16×16 , and take again coarse grids of size 10×10 , 20×20 , and 40×40 . Note that now in fact the resolution h is reduced as H is reduced to $1/h = 160$, 320, and finally 640. As can be seen, HE0 = ME1 shows continued good approximation as

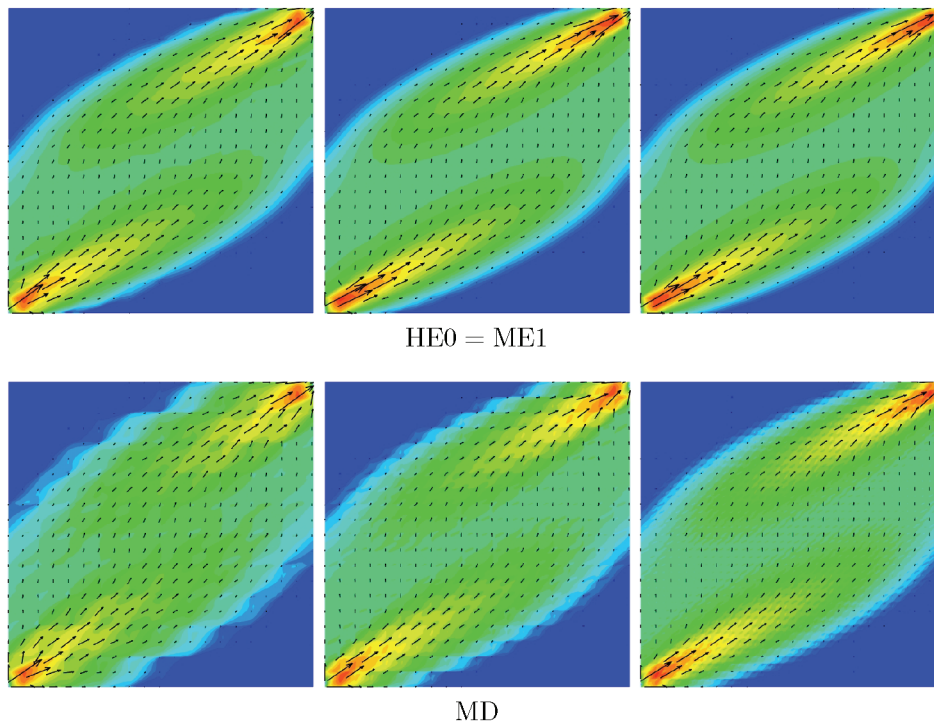


FIG. 7.3. Anisotropic test. The upscaled HE0 = ME1 (top) and MD (bottom) solution using coarse 10×10 , 20×20 , and 40×40 grids, respectively, from left to right, and fixed 16×16 subgrids.

TABLE 7.2

Anisotropic test. Relative errors in the pressure and velocity for HE0 = ME1 and MD relative to the 160×160 reference BDM1 solution. Discrete ℓ^2 -norm errors are shown.

Coarse mesh $N \times N$	Subgrid mesh $n \times n$	Resolution Nn	Discrete ℓ^2 velocity error	
			HE0	MD
10	16	160	0.2704	0.4225
20	16	320	0.0686	0.2863
40	16	640	0.0377	0.1671
80	16	1280	0.0353	0.1257
40	4	160	0.0200	0.1545
80	4	320	0.0307	0.1040
160	4	640	0.0345	0.1122

$H \rightarrow 0$. However, MD exhibits a stronger fluctuation effect compared to Figure 7.2, even on the finest grid.

In Table 7.2 we compare the relative errors as computed in the discrete ℓ^2 -norm (i.e., we compute the relative error using a trapezoidal rule for the integrals, and thus the numbers differ slightly from the previous table). We show results for both 16×16 and 4×4 subgrids. As can be seen, the errors are either negligible or improve with refinement for HE0 = ME1. For MD, the finer subgrid has the slightly greater error, but perhaps this is not conclusive. This example shows how small the twisted basis function effect is on the error, and perhaps explains why the MD element works well in practical computations.

7.2. A streaked permeability. Our second set of computational tests is related to the previous anisotropic case. We work again on the unit square $\Omega = (0, 1)^2$ with an injection well in the lower left corner covering $(0, 1/20)^2$ and a production well of opposite strength in the upper right corner covering $(1 - 1/20, 1)^2$. We consider now three locally isotropic but heterogeneous permeability fields, on grids of size 40×40 , 80×80 , and 160×160 . The permeability fields alternate the values 1 and 200 over the grid in a streaked pattern, as illustrated in Figure 7.4. In each case, the “streak” is about one cell wide, so we have, respectively for the grids, an increasing number of about 20, 40, and 80 streaks which decrease in width.

The angle of these streaks is exactly $\tan \theta = 1/2$ (i.e., $\theta = 26.565$), the same as in the previous test case. Moreover, the arithmetic and harmonic means of 1 and 200 are 100.5 and 1.990. Thus, up to the stair-step nature of the permeability streaks, these

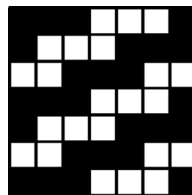


FIG. 7.4. Streaked test. The permeability pattern as illustrated on a 7×7 grid. The streaks, of about one cell wide, extend across the domain at angle $\tan \theta = 1/2$. The streaks alternate permeability between the two values 200 (black) and 1 (white).

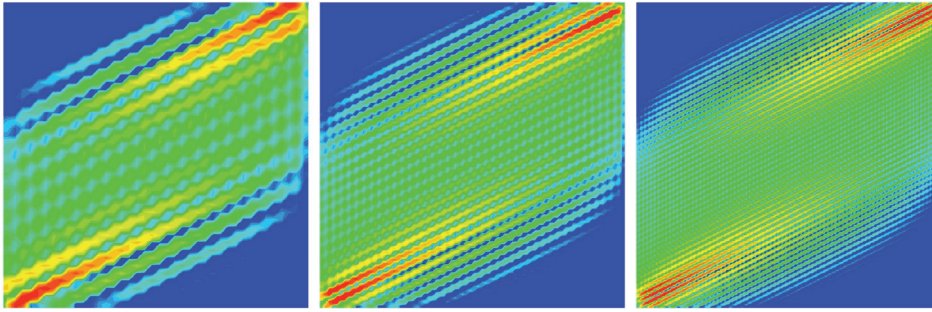


FIG. 7.5. *Streaked test. The fine-scale BDM1 solution for grids of size 40×40 , 80×80 , and 160×160 , from left to right. The color depicts the speed, on a log scale from $4.6e-4$ (blue) to $4.6e-2$ (red).*

fields homogenize into the anisotropic tensor treated in the previous set of computational tests.

The fine-scale BDM1 solution is shown in Figure 7.5, wherein we plot only the speed of the velocity field, since the stair-step nature of the velocity arrows obscures the depiction of the flow direction. Note that the flow speed closely matches that of the homogenized case Figure 7.1, except that we see explicit streaks. Moreover, the speed appears to converge to the anisotropic case as the grid spacing tends to zero.

In Figures 7.6 and 7.7 we show the solution for HE0 and for HE0-OS, which uses oversampling to define \mathcal{A}_ϵ . From left to right, the columns correspond to the 40×40 , 80×80 , and 160×160 fine grids. The top row uses a fixed 8×8 subgrid (so the coarse grids are 5×5 , 10×10 , and 20×20 , respectively), and the bottom row uses a fixed 4×4 subgrid (so the coarse grids are 10×10 , 20×20 , and 40×40 , respectively). Both

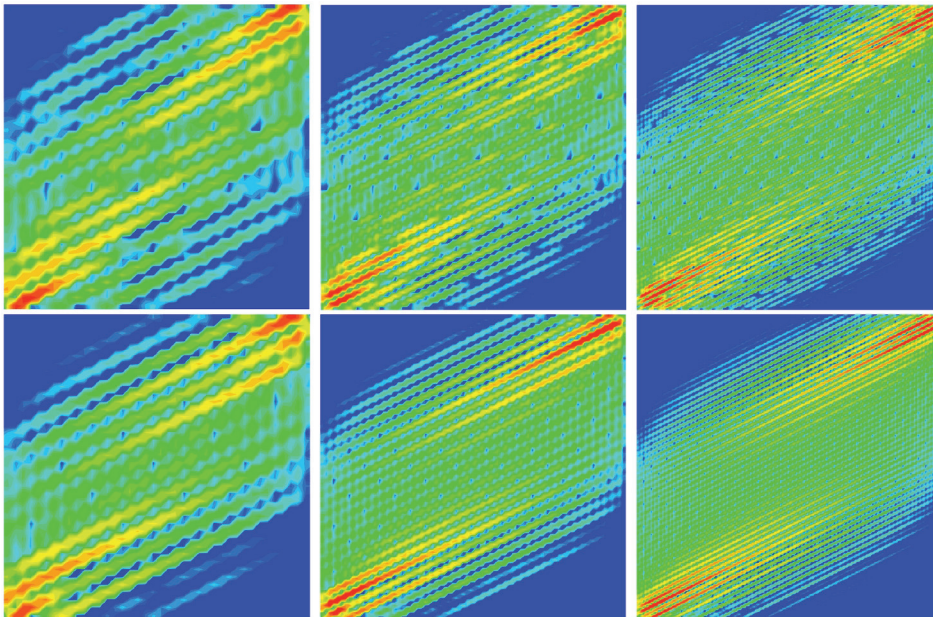


FIG. 7.6. *Streaked test. The upscaled HE0 speed. The top row uses 5×5 , 10×10 , and 20×20 coarse grids, from left to right, with a fixed 8×8 subgrid. The bottom row uses 10×10 , 20×20 , and 40×40 coarse grids, with a fixed 4×4 subgrid.*

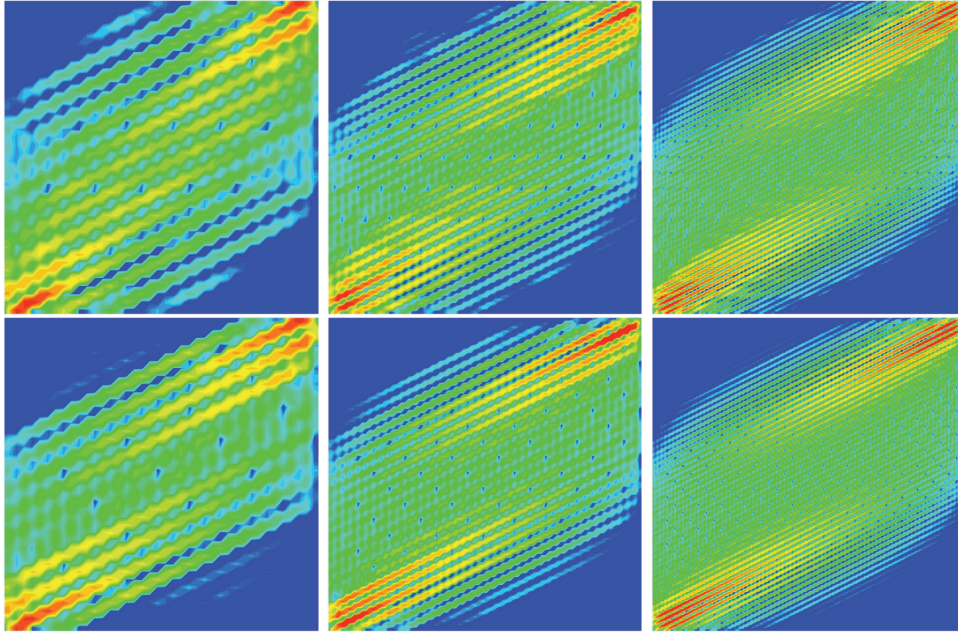


FIG. 7.7. *Streaked test. The upscaled HE0-OS speed. The top row uses 5×5 , 10×10 , and 20×20 coarse grids, from left to right, with a fixed 8×8 subgrid. The bottom row uses 10×10 , 20×20 , and 40×40 coarse grids, with a fixed 4×4 subgrid.*

the HE0 and HE0-OS solutions closely approximate the fine-scale solution (Figure 7.5), and show nice improvement as H is reduced. The oversampled version is clearly better.

The corresponding solution for MD is shown in Figure 7.8. Compared to HE0-OS, we see relatively poorer approximation in at least two ways. First, MD appears to be more numerically diffusive: the speed is washed out and spread over the domain compared to HE0-OS. Second, the MD velocity along the permeability streaks is disjointed, while HE0-OS shows no such effect. In fact, MD exhibits a fluctuation across the domain similar to that seen in the anisotropic test example (e.g., as in Figures 7.2 and 7.3), and this fluctuation appears related to the disjointedness of the speed (i.e., the color bands are disjoint). Even though the permeability is locally isotropic, MD has difficulty with this problem because, on the coarser scales, there is an induced anisotropy from the subgrid which, as we saw, the method cannot approximate well.

7.3. A moderately heterogeneous permeability. Our third numerical test case is based on a moderately heterogeneous, mildly correlated, but locally isotropic permeability field that was geostatistically generated on a uniform 40×40 grid, as depicted in Figure 7.9. The test is an example of a quarter five-spot pattern of wells, with wells in the lower right and upper left corners. The domain is 40 meters square. This is a good test of the methods, since even though the scale separation assumption (4.1) does not strictly hold, the mild correlation does suggest that we are not too far from local periodicity.

Since this is a moderate test case, all methods work reasonably well, except possibly ME0. Relative errors are given in Table 7.3. Note that RT0 exhibits about 3% error compared to BDM1, even though both computations are done on the fine scale, due to discontinuities in the permeability. Omitting ME0, the multiscale elements show ℓ^2 pressure errors of about 10–14% and velocity errors of about 12–19%, which is

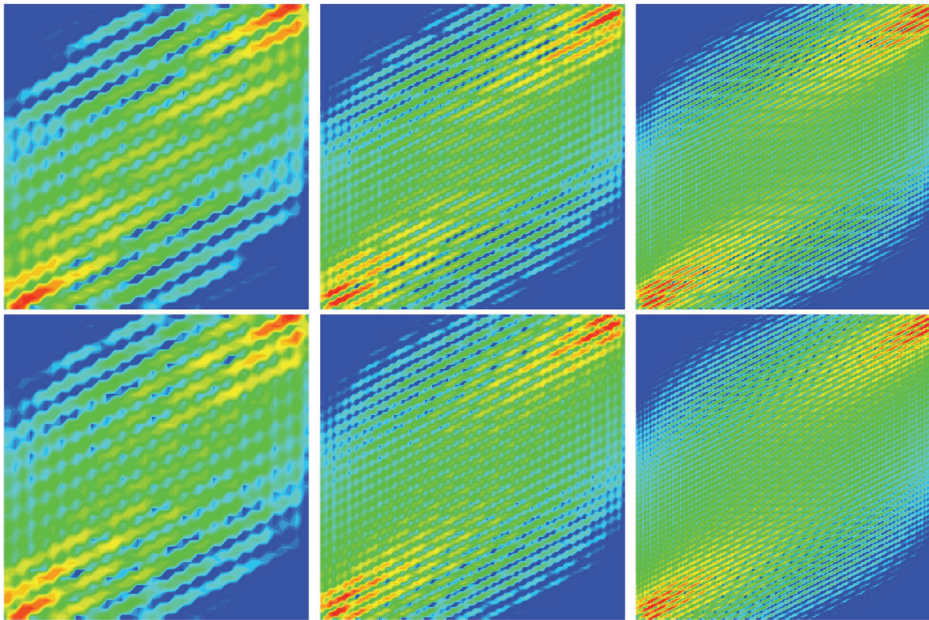


FIG. 7.8. Streaked test. The upscaled MD speed. The top row uses 5×5 , 10×10 , and 20×20 coarse grids, from left to right, with a fixed 8×8 subgrid. The bottom row uses 10×10 , 20×20 , and 40×40 coarse grids, with a fixed 4×4 subgrid.

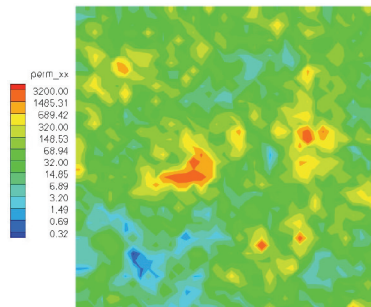


FIG. 7.9. Moderate heterogeneity test. The permeability field on a 40×40 grid. The permeability is depicted on a log scale, and varies from about 0.32 to 3200 millidarcy.

TABLE 7.3

Moderate heterogeneity test. Relative errors in the pressure and velocity for various elements relative to the 40×40 reference BDM1 solution, using a 4×4 coarse grid (and 10×10 subgrid), except that RT0 is a fine-grid result. Both ℓ^2 and ℓ^∞ (maximum) norm errors are shown.

Method	Pressure error		Velocity error	
	ℓ^2	ℓ^∞	ℓ^2	ℓ^∞
RT0	0.0357	0.0297	0.0297	0.0281
ME0	0.1606	0.2087	0.2872	0.2587
ME1	0.1031	0.1623	0.1873	0.1646
MD	0.1384	0.2362	0.1582	0.1236
HE0	0.1338	0.2008	0.1444	0.1374
HE0-OS	0.1405	0.1935	0.1180	0.1053

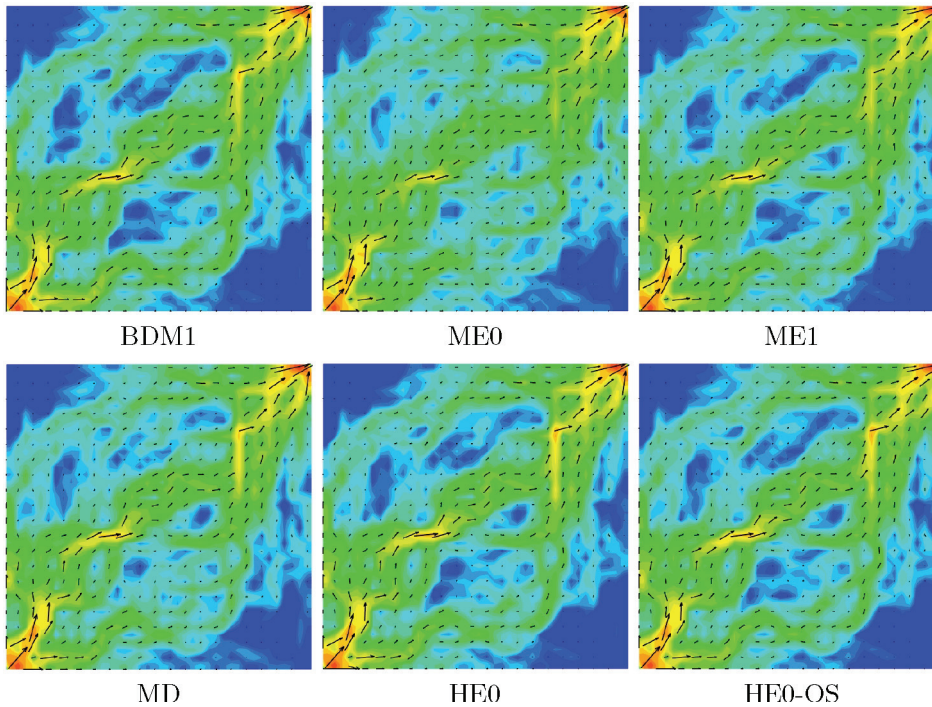


FIG. 7.10. *Moderate heterogeneity test. The top row shows the solution using fine BDM1 and upscaled ME0 and ME1 elements. The bottom row uses upscaled MD, HE0, and HE0-OS elements. The fine grid is 40×40 , and the upscaled results use a 4×4 coarse grid with 10×10 subgrid. The color depicts the speed, on a log scale from 0.55 to 0.0055, and the arrows show the velocity.*

probably reasonable for engineering accuracy in subsurface flow applications (given our lack of permeability characterization). The oversampled HE0-OS gives the best velocity, while interestingly, ME1 gives the best pressure and worst velocity. In Figure 7.10 we show the velocities of the various methods.

7.4. A simple channelized permeability. It is known that local upscaling or multiscale methods have difficulty treating permeabilities that exhibit long-range correlations, such as high permeability channels (see, e.g., [2]), which are far from locally periodic. These are good tests of the HE0 method, since its derivation suggests it will work well in the two-scale separation case of (4.1), but it is unclear how well it extends to problems with more general permeability fields. We consider a relatively simple synthetic example taken from White and Horne [45]. The permeability, depicted in Figure 7.11, takes only three values on a fine 30×30 grid and exhibits a single fluvial channel of high permeability. We again consider a quarter five-spot pattern of wells, with wells in the lower right and upper left corners. The fine-scale BDM1 solution is shown in Figure 7.12, wherein it is clear that fluid concentrates into the high permeability channel and tends to avoid the lowest permeability regions.

We upscale these results to a very coarse 3×3 grid that clearly does not resolve the channel. Nevertheless, as seen in Figure 7.13, the HE0-OS, HE0, and MD methods are able to properly resolve the channel flow. Errors are given in Table 7.4, where it is verified that the HE0-OS solution is best, giving a 15% relative ℓ^2 velocity error.

From Figure 7.13, the main differences in the solutions are in the lower central coarse element, which is where fluids concentrate as they enter the high permeability

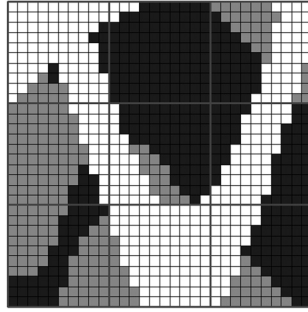


FIG. 7.11. *Simple channel test. Shown is the fine 30×30 grid permeability, which has only three values: 10 (white), 1 (gray), and 0.1 (black) darcies. Upscaling to a coarse 3×3 grid does not resolve the high permeability channel.*

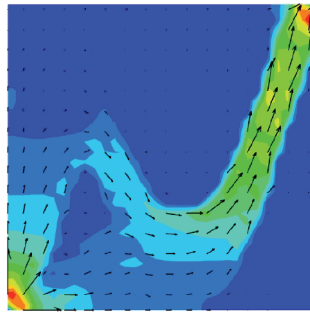


FIG. 7.12. *Simple channel test. Shown is the fine 30×30 grid BDM1 solution. The color depicts the speed (not on a log scale), and the arrows show the velocity direction (and speed).*

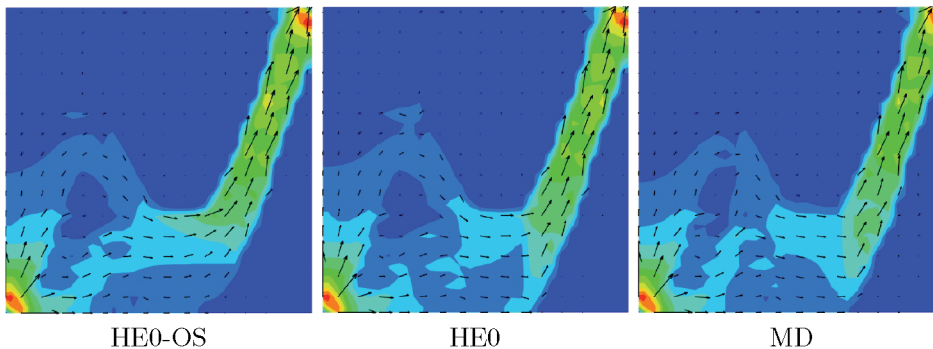


FIG. 7.13. *Simple channel test. Shown are the upscaled HE0-OS, HE0, and MD solutions for a 3×3 coarse grid with 10×10 subgrid. The color depicts the speed (not on a log scale), and the arrows show the velocity direction (and speed).*

channel. In Figure 7.14 we explore the performance of HE0-OS, HE0, and MD near the right-most (\mathbf{e}_1) and upper (\mathbf{e}_2) edges of this coarse element. We show the basis functions on these edges that are used to produce the solution over this coarse element. We can see that the MD element on \mathbf{e}_1 is far too uniform compared to what is needed from the BDM1 fine-scale solution. Moreover, the MD element on \mathbf{e}_2 overemphasizes the flow

TABLE 7.4

Simple channel test. Relative errors in the pressure and velocity for various elements relative to the 30×30 reference BDM1 solution, using a 3×3 coarse grid (and 10×10 subgrid), except that RT0 is a fine-grid result. Both ℓ^2 and ℓ^∞ (maximum) norm errors are shown.

Method	Pressure error		Velocity error	
	ℓ^2	ℓ^∞	ℓ^2	ℓ^∞
RT0	0.0148	0.0200	0.0251	0.0387
ME0	1.1023	0.1808	0.4663	0.3393
ME1	0.4905	0.1198	0.2749	0.3228
MD	0.3049	0.1015	0.2619	0.3624
HE0	0.2784	0.0660	0.2043	0.3080
HE0-OS	0.2811	0.0711	0.1524	0.2202

on the left compared to flow on the right (the flow is also opposite, but this is immaterial since it has a negative weight in the solution).

On the other hand, the HE0-OS elements do a much better job representing the BDM1 flow. On \mathbf{e}_1 we show the primary basis function $\mathbf{v}_{e_1}^1$ for flow in the x -direction above the basis function $\mathbf{v}_{e_1}^2$ for the cross-flow in the y -direction. Both functions show a good multiscale shape for the fine-scale flow. In fact, the cross-flow weight is about 2.5 times the primary flow weight. On \mathbf{e}_2 we show the primary basis function $\mathbf{v}_{e_1}^2$ for flow in the y -direction to the left of the basis function $\mathbf{v}_{e_1}^1$ for the cross-flow. In this case the primary flow has the greater weight (in absolute value).

Since oversampling uses information outside E_e , we also show the nonoversampled HE0 elements, which use no more information than MD. Note that from Table 7.4, HE0 is about 20% accurate, while MD is only 26% accurate. This is seen in the basis functions, which better represent the fine BDM1 solution. Interestingly, the strength of the weights for primary versus cross-flow is opposite that for HE0-OS: on \mathbf{e}_1 the primary flow is more important while on \mathbf{e}_2 it is the cross-flow. The point is, since MD only uses a type of primary flow, it cannot do as well as HE0 or HE0-OS, which significantly use the cross-flow basis functions.

7.5. A channelized permeability from SPE10. In our final test case, we take our permeability field from one layer of the tenth Society of Petroleum Engineers (SPE) comparative solution project (SPE10) [19]. These are extremely difficult, channelized test cases, which are very far from locally periodic. We thus expect significant error for the purely local methods considered in this paper. The permeability is anisotropic, but the anisotropy is aligned with the coordinate axes, so no local twisting effect arises. We take layer 85, which is shown in Figure 7.15. It is given on a fine 60×220 grid. Our upscaled results will be computed over a coarse 6×22 grid with a 10×10 subgrid.

The fine-scale BDM1 speed is shown in Figure 7.16, which should be compared to the upscaled results in Figure 7.17 for MD, HE0-OS (oversampled), HE0, and ME1. Note the existence of strong, long-range channels. All elements appear to work well.

The relative errors are given in Table 7.5. Note first that the discrepancy between BDM1 and RT0, which are both fine-scale results, is about 8% in ℓ^2 , so this is a very difficult problem to approximate well even when the permeability is fully resolved by the grid. Again, the difficulty is related to the fact that the permeability is discontinuous. We might reduce this discrepancy by using a finer mesh; however, if we did so, the physical application would demand a downscaling of the permeability field to the refined

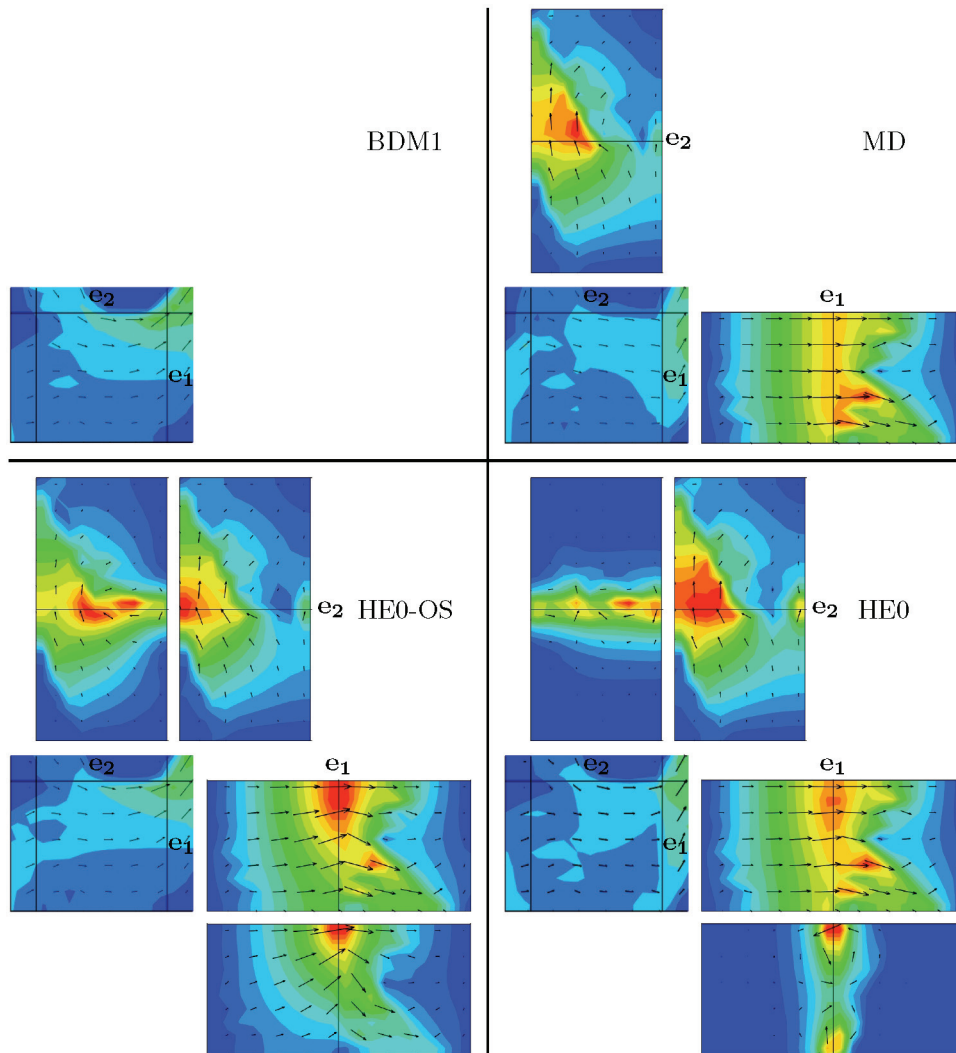


FIG. 7.14. Simple channel test. Shown are the multiscale basis functions for MD, HE0-OS, and HE0 near the right-most (\mathbf{e}_1) and upper (\mathbf{e}_2) edges of the lower center coarse element. For HE0-OS and HE0, on \mathbf{e}_1 , we show the primary basis function for flow in the x -direction above the basis function for the cross-flow in the y -direction, and on \mathbf{e}_2 , we show the primary basis function for flow in the y -direction to the left of the basis function for the cross-flow.

mesh. Since the downscaling process is not well understood, we simply compute on the 60×220 grid, note the extreme difficulty of the problem, and realize that the error is within engineering accuracy for the problem, given the practical uncertainty in the permeability data.

Now note in Table 7.5 that HE0 without oversampling is disappointing, giving a large 70% error. From Figure 7.17, we see that it does not correctly compute the channel near the top center of the domain. However, oversampling corrects this and gives the best error, which is nevertheless somewhat large at 35%.

Large errors in the relative ℓ^2 norm are surprising, since Figure 7.17 suggests good approximation. Perhaps this norm is a poor measure of velocity error. Generally speak-

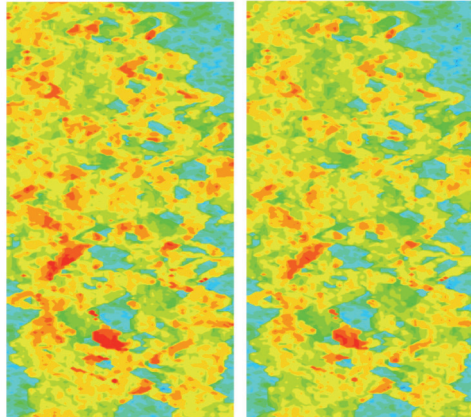


FIG. 7.15. *SPE10-85 test. The x and y permeability fields on a 60×220 grid using a log scale from $1.9e-11$ (red) to $1.0e-18$ (blue) square meters.*

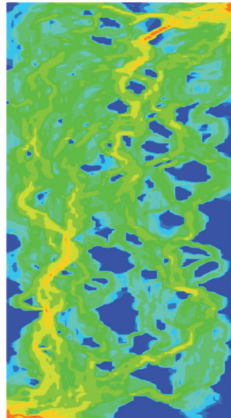


FIG. 7.16. *SPE10-85 test. The fine-scale BDM1 speed on a 60×220 grid using a log scale from $6.0e-6$ (red) to $6.0e-9$ (blue).*

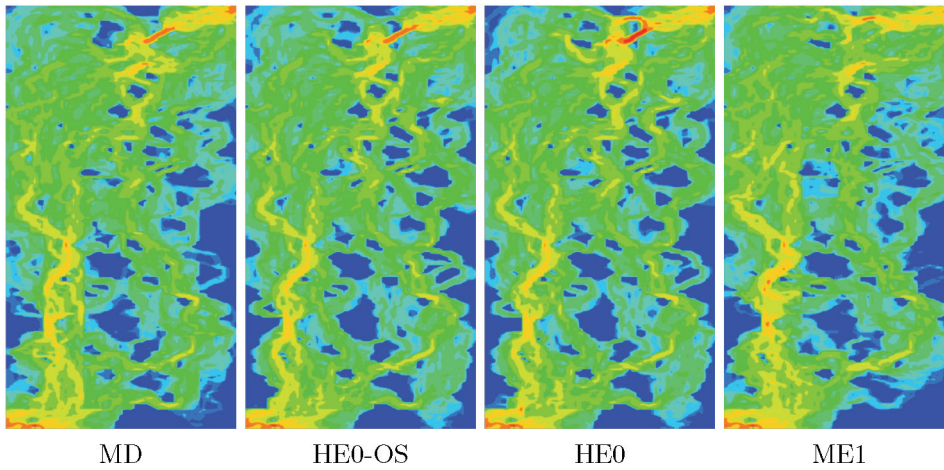


FIG. 7.17. *SPE10-85 test. The speed on a 6×22 coarse grid with a 10×10 subgrid using various elements.*

TABLE 7.5

SPE10-85 test. Relative errors in the pressure and velocity for various elements relative to the 60×220 reference BDM1 solution, using a 6×22 coarse grid (and 10×10 subgrid), except that RT0 is a fine-grid result. Both ℓ^2 and ℓ^∞ (maximum) norm errors are shown. Also given are relative ℓ^2 errors in the tracer concentration on a 60×220 grid using the various velocity fields, compared to the tracer computed using the fine-grid BDM1 velocity.

Method	Pressure error		Velocity error		Tracer error
	ℓ^2	ℓ^∞	ℓ^2	ℓ^∞	ℓ^2
RT0	0.0383	0.0265	0.0777	0.1419	—
ME0	0.2657	0.1013	0.7196	0.5333	—
ME1	0.2165	0.0756	0.5750	0.5623	0.4116
MD	0.2385	0.1111	0.4511	0.4618	0.3009
HE0	0.2414	0.1083	0.6961	0.9063	0.2046
HE0-OS	0.2402	0.1057	0.3492	0.5549	0.1793

ing in porous medium applications, velocities are computed to transport some fluid such as a tracer. We computed simple linear tracer transport using the steady-state computed flow fields and a small amount of diffusion, until tracer filled about half the domain. The relative errors for tracer concentration are also given in Table 7.5. These show a more reasonable error of about 18% for velocities computed using HE0-OS, which is the best of the methods tested.

We remark that layer 36 of the SPE10 set produces about 48% error for HE0 and HE0-OS, and a bit more for the other methods. Moreover, tracer errors were about 50% for this permeability. Unlike layer 85, this layer has a single strong channel, which is very hard to identify and approximate well with a purely local method such as the ones used herein.

8. Summary and conclusions. In this paper, we defined and evaluated several existing mixed multiscale finite element methods. These all approximate the pressure by a piecewise constant over the coarse mesh. Moreover, each method defines the velocity basis functions on an edge e by solving the differential equation locally over the support E_e , using homogeneous Neumann boundary conditions on the outer boundaries ∂E_e . They differ in the way the normal velocity is defined on e .

The standard multiscale elements ME0 and ME1 impose a polynomial normal velocity on e of degree 0 or 1, respectively, and solve for the basis function on each adjoining element $E_{e,i}$ separately. These methods have 1 and 2 dof's per edge (in two dimensions), respectively. The dual-support element MD simply solves the differential system locally over all of E_e , which implicitly defines the normal velocity on e . It has only 1 dof per edge.

New elements based on homogenization theory HE0 were presented. These define the normal velocity on e based on the multiscale expansion predicted by homogenization, which is that the normal velocity is a fine-scale function \mathcal{A}_e multiplied by a smooth function (the homogenized velocity). Therefore, to define the multiscale basis, the normal velocity on e is approximated by this multiplier function times a (vector) polynomial of degree 0. The method uses 2 dof's per edge (in two dimensions). The multiplier function is obtained by solving local periodic cell problems in each direction: the primary direction normal to e and cross-flow along e . The domain for the cell problems is naturally set to be E_e , although other domains could be used. When a larger domain is used, we referred to the variant as having oversampled elements HE0-OS.

We showed by a family of counterexamples that MD cannot converge in any sense as $H \rightarrow 0$. The problem is anisotropy in the permeability, since in this case, as $H \rightarrow 0$, the MD elements do not have a constant normal velocity on e and therefore cannot approximate smooth functions.

The numerical test cases showed that generally HE0-OS outperforms the other methods. The anisotropic twisting effect for MD was shown in the first test case using a constant but anisotropic permeability. A fine-scale fluctuation was evident due to the nonsmoothness of the basis as $H \rightarrow 0$. However, it is a relatively small effect, possibly explaining at least partly why the MD elements generally work well in practical applications. This anisotropic case was mimicked through a locally isotropic permeability of streaks that homogenize to the anisotropic case. The fluctuations in the MD solution were evident, and caused the solution to appear disjointed along the streaks.

All the multiscale methods, except possibly ME0, seemed to work well for moderate levels of heterogeneity, as shown in the third test case. Channelized flow is difficult to approximate with purely local multiscale methods. The simple channelized test case showed that better results were obtained using HE0 and HE0-OS over MD, because the former two methods include basis functions that approximate cross-flow, whereas MD only approximates primary flow.

The final test case using a very complex channelized permeability from the SPE10 comparative solution project was extremely challenging for these purely local multiscale methods. The relative ℓ^2 velocity errors were quite large, even though the graphs of the velocity fields appeared reasonable. However, it is not completely clear that this is a good measure of the error. Since in applications computed velocities are often used in transport problems, perhaps a better norm is to consider the effect of the velocity errors on transport. A simple linear tracer transport test showed relative ℓ^2 concentration errors to be more reasonable.

The theoretical results in the appendix below present a convergence proof for ME0 and ME1 that reduces to four simple steps. The MD elements fail only to approximate smooth solutions, which is the basis of our counterexample. While the proof is not extended to HE0 elements because of technical issues related to homogenization theory, it is pointed out below that HE0 elements do not fail to approximate smooth solutions. Thus there is some theoretical basis for expecting that HE0 should work well, as our numerical results also showed.

Appendix. Theoretical convergence results. In this appendix we prove convergence of the methods ME0 and ME1 under the two-scale separation hypothesis (4.1). These results are known [18], [7], but we include this appendix since the style of proof developed here is simpler than appears in the literature, and is therefore a useful guide in devising new multiscale elements. We also show where the proof breaks down for MD elements, and speculate on the case of HE0 elements.

In this appendix, we assume that \mathcal{T}_H is a quasi-uniform rectangular grid of maximal spacing $H > 0$. That is, for positive constants c and C , and any $E \in \mathcal{T}_H$ and $e \in \mathcal{E}_H$,

$$cH^d \leq |E| \leq CH^d \quad \text{and} \quad cH^{d-1} \leq |e| \leq CH^{d-1}.$$

We assume that the coefficient $a_\epsilon(x)$ is smooth, bounded, and uniformly positive definite symmetric. That is, there are positive constants a_* and a^* , independent of ϵ , such that for any $\xi \in \mathbb{R}^d$,

$$(A.1) \quad a_* |\xi|^2 \leq \xi \cdot \alpha_\epsilon(x) \xi \leq a^* |\xi|^2 \quad \forall x \in \Omega.$$

Let \mathcal{P}_{W_H} denote L^2 -projection onto W_H . It is well known that the conforming approximation (2.3)–(2.4) to (2.1)–(2.2) is *quasi-optimal*, no matter which conforming finite elements are used (provided only that $\nabla \cdot \mathbf{V}_H \subset W_H$).

LEMMA A.1. *If (A.1) holds and $\nabla \cdot \mathbf{V}_H \subset W_H$, then*

$$(A.2) \quad \|\mathbf{u}_\epsilon - \mathbf{u}_H\|_0 \leq \sqrt{\frac{a^*}{a_*}} \|\mathbf{u}_\epsilon - \mathbf{v}\|_0$$

for any $\mathbf{v} \in \mathbf{V}_H$ such that $\nabla \cdot \mathbf{v} = \mathcal{P}_{W_H} \nabla \cdot \mathbf{u}_\epsilon$.

The proof follows from subtracting (2.3)–(2.2) from (2.1)–(2.2), which leads to the equation for the error

$$(A.3) \quad (\alpha_\epsilon(\mathbf{u}_\epsilon - \mathbf{u}_H), \mathbf{v}) - (\mathcal{P}_{W_H} p - p_H, \nabla \cdot \mathbf{v}) = 0 \quad \forall \mathbf{v} \in \mathbf{V}_H,$$

$$(A.4) \quad (\nabla \cdot (\mathbf{u}_\epsilon - \mathbf{u}_H), w) = 0 \quad \forall w \in W_H,$$

and replacing \mathbf{v} by $(\mathbf{u}_\epsilon - \mathbf{v}) - (\mathbf{u}_\epsilon - \mathbf{u}_H) \in \mathbf{V}_H$ and w by $\mathcal{P}_{W_H} p - p_H \in W_H$. Then

$$(\alpha_\epsilon(\mathbf{u}_\epsilon - \mathbf{u}_H), \mathbf{u}_\epsilon - \mathbf{u}_H) = (\alpha_\epsilon(\mathbf{u}_\epsilon - \mathbf{u}_H), \mathbf{u}_\epsilon - \mathbf{v})$$

for any $\mathbf{v} \in \mathbf{V}_H$ with $\nabla \cdot \mathbf{v} = \mathcal{P}_{W_H} \nabla \cdot \mathbf{u}_\epsilon$.

In light of Lemma A.1, our goal in a convergence analysis is to find any good approximation of \mathbf{u}_ϵ in our multiscale finite element space that respects the divergence condition.

A.1. Homogenized finite elements. The ϵ dependence of our finite elements is difficult to analyze directly, so we define smooth (homogenized) versions. The idea is to replace the true coefficient a_ϵ with the corresponding homogenized one a_0 in the definitions of the finite elements (2.13)–(2.15), (6.1)–(6.3), and (2.18)–(2.20). This gives the solutions $\mathbf{v}_{0,e}^{ME0}$, $\mathbf{v}_{0,e}^{ME1,i}$, and $\mathbf{v}_{0,e}^{MD}$, respectively. From these basis functions we define the spaces

$$\mathbf{V}_{0,H}^M = \text{span}_{e \in \mathcal{E}_H} \left\{ \mathbf{v}_{0,e}^M \right\}, \quad M = \text{ME0, MD}, \quad \text{and} \quad \mathbf{V}_{0,H}^{ME1} = \text{span}_{e \in \mathcal{E}_H, i} \left\{ \mathbf{v}_{0,e}^{ME1,i} \right\}.$$

To unify notation, we will henceforth include i , which ranges over the number of basis functions on e , in the notation, though there is only one value for i ($i = 1$) when $M = \text{ME0}$ or MD .

Since our finite elements are defined by boundary value problems, the homogenization result Theorem 4.1 applies. The following result is a direct application of the theorem, since the coefficient in the differential equations is a_ϵ and the multiscale and homogenized elements use the same fixed boundary conditions.

LEMMA A.2. *Assuming (4.1), for each $e \in \mathcal{E}_H$ and method $M = \text{ME0, ME1, and MD}$,*

$$(A.5) \quad \mathbf{v}_e^{M,i} = \mathcal{A}_\epsilon \mathbf{v}_{0,e}^{M,i} + \theta_\epsilon^{E,M,i},$$

where

$$(A.6) \quad \|\theta_\epsilon^{E,M,i}\|_{0,E_e} \leq C \{ \epsilon \|\mathbf{v}_{0,e}^{M,i}\|_{1,E_e} + \sqrt{\epsilon |\partial E_e|} \|\mathbf{v}_{0,e}^{M,i}\|_{0,\infty,E_e} \}.$$

A.2. Some flux-based projection operators. For the analysis, we define some projection operators related to the Raviart–Thomas or Fortin projection operators [42],

[17]. It is convenient for the notations to assume that $L_1 = 1$ and the rest of the L_i form an orthogonal basis for $L^2(e)$, normalized so that $\int_e L_i^2 ds = |e|$.

Given a vector function $\mathbf{v} \in H(\operatorname{div}; \Omega) \cap L^r(\Omega)$, for some $r > 2$, on Ω , for each $e \in \mathcal{E}_H$, let

$$(A.7) \quad \gamma_e^i = \frac{1}{|e|} \int_e \mathbf{v} \cdot \nu_e L_i ds.$$

Then the Raviart–Thomas and BDM projection operators are defined by

$$(A.8) \quad \pi^M \mathbf{v} = \sum_{e \in \mathcal{E}_{H,i}} \gamma_e^i \mathbf{v}_e^{M,i}, \quad M = \text{RT0, BDM1}.$$

Similarly, for each multiscale method $M = \text{ME0, ME1, and MD}$, we define $\pi_\epsilon^M \mathbf{v} \in \mathbf{V}_H^M$ and $\pi_0^M \mathbf{v} \in \mathbf{V}_{0,H}^M$ by

$$(A.9) \quad \pi_\epsilon^M \mathbf{v} = \sum_{e \in \mathcal{E}_{H,i}} \gamma_e^i \mathbf{v}_e^{M,i} \quad \text{and} \quad \pi_0^M \mathbf{v} = \sum_{e \in \mathcal{E}_{H,i}} \gamma_e^i \mathbf{v}_{0,e}^{M,i}.$$

The following lemma is easy to verify.

LEMMA A.3. For $\mathbf{v} \in H(\operatorname{div}; \Omega) \cap L^r(\Omega)$, $r > 2$, and $M = \text{ME0, ME1, or MD}$,

$$(A.10) \quad \int_e \pi_\epsilon^M \mathbf{v} \cdot \nu ds = \int_e \pi_0^M \mathbf{v} \cdot \nu ds = \int_e \pi^{\text{RT0}} \mathbf{v} \cdot \nu ds = \int_e \mathbf{v} \cdot \nu ds \quad \forall e \in \mathcal{E}_H,$$

$$(A.11) \quad (\nabla \cdot \pi_\epsilon^M \mathbf{v}, w) = (\nabla \cdot \pi_0^M \mathbf{v}, w) = (\nabla \cdot \pi^{\text{RT0}} \mathbf{v}, w) = (\nabla \cdot \mathbf{v}, w) \quad \forall w \in W_H.$$

The last result is that $\nabla \cdot \pi_\epsilon^M = \nabla \cdot \pi_0^M = \nabla \cdot \pi^{\text{RT0}} = \mathcal{P}_{W_H} \nabla \cdot$.

We turn now to an abstract multiscale approximation result.

LEMMA A.4. Assuming (4.1), if $\mathbf{v} \in H^1(\Omega)$, then for $M = \text{ME0, ME1, or MD}$,

$$(A.12) \quad \|\pi_\epsilon^M \mathbf{v} - \mathcal{A}_\epsilon \pi_0^M \mathbf{v}\|_0 \leq C \|\mathbf{v}\|_1 (\epsilon/H + |\sqrt{\epsilon/H}|).$$

Proof. We begin with a stability result. The quasi-uniformity of the mesh \mathcal{T}_H and our normalization gives that

$$\|L_i\|_{0,\infty,e} \leq CH^{-(d-1)/2} \|L_i\|_{2,e} = CH^{-(d-1)/2} |e|^{1/2} \leq C,$$

where C is independent of the domain size (i.e., H), so with (A.7) defining γ_e^i , we compute

$$(A.13) \quad \begin{aligned} |\gamma_e^i| &\leq \frac{1}{|e|} \int_e |\mathbf{v} \cdot \nu_e| ds \|L_i\|_{0,\infty,e} \leq \frac{C}{|e|} \left(\frac{1}{H} \int_{E_e} |\mathbf{v}| dx + \int_{E_e} |\nabla \mathbf{v}| dx \right) \\ &\leq C \frac{|E_e|^{1/2}}{H|e|} \|\mathbf{v}\|_{1,E_e} \leq CH^{-d/2} \|\mathbf{v}\|_{1,E_e}. \end{aligned}$$

Now Lemma A.2 implies that

$$\pi_\epsilon^M \mathbf{v} - \mathcal{A}_\epsilon \pi_0^M \mathbf{v} = \sum_{e \in \mathcal{E}_{H,i}} \gamma_e^i (\mathbf{v}_e^{M,i} - \mathcal{A}_\epsilon \mathbf{v}_{0,e}^{M,i}) = \sum_{e \in \mathcal{E}_{H,i}} \gamma_e^i \theta_e^{E_e, M, i},$$

and, further,

$$\begin{aligned} \|\pi_\epsilon^M \mathbf{v} - \mathcal{A}_\epsilon \pi_0^M \mathbf{v}\|_{0,E} &\leq \sum_{e \subset \partial E, i} |\gamma_e^i| \|\theta_e^{E, M, i}\|_{0,E} \\ &\leq \sum_{e \subset \partial E, i} |\gamma_e^i| \{ \epsilon \|\mathbf{v}_{0,e}^{M,i}\|_{1,E_e} + \sqrt{\epsilon |\partial E_e|} \|\mathbf{v}_{0,e}^{M,i}\|_{0,\infty,E_e} \}. \end{aligned}$$

Elliptic regularity of the problems defining the finite elements (i.e., (2.13)–(2.15), (6.1)–(6.3), or (2.18)–(2.20) with a_ϵ replaced by a_0) and the quasi-uniformity of the mesh \mathcal{T}_H imply that

$$\|\mathbf{v}_{0,e}^M\|_{1,E_e} \leq CH^{d/2-1}.$$

Moreover, the smoothness of a_0 implies that $\|\mathbf{v}_{0,e}^M\|_{0,\infty,E_e} \leq C$. Thus, using (A.13),

$$\begin{aligned} \|\pi_\epsilon^M \mathbf{v} - \mathcal{A}_\epsilon \pi_0^M \mathbf{v}\|_0^2 &\leq C \sum_{E \in \mathcal{T}_H} \left\{ \sum_{e \subset \partial E, i} |\gamma_e^i| (\epsilon H^{d/2-1} + \sqrt{\epsilon H^{d-1}}) \right\}^2 \\ &\leq C \sum_{e \in \mathcal{E}_H, i} |\gamma_e^i|^2 H^d (\epsilon/H + \sqrt{\epsilon/H})^2 \\ &\leq C \sum_{e \in \mathcal{E}_H} \|\mathbf{v}\|_{1,E_e}^2 (\epsilon/H + \sqrt{\epsilon/H})^2 \\ &\leq C \|\mathbf{v}\|_1^2 (\epsilon/H + \sqrt{\epsilon/H})^2, \end{aligned}$$

which completes the proof. \square

We also need the following smooth approximation result.

LEMMA A.5. *For any \mathbf{v}_0 that has the form $\mathbf{v}_0 = -a_0 \nabla \phi_0$ for some $\phi_0 \in H^2(\Omega)$,*

$$(A.14) \quad \|\mathbf{v}_0 - \pi_0^M \mathbf{v}_0\|_0 \leq C \|\mathbf{v}_0\|_j H^j,$$

where $M = \text{ME0}$ and $j = 1$ or $M = \text{ME1}$ and $j = 1, 2$.

The counterexamples of section 3 show that a similar result cannot hold in general for MD.

Proof. On an element $E \in \mathcal{T}_H$, with $e \subset \partial E$ and

$$\gamma_e^i = \frac{1}{|e|} \int_e \mathbf{v}_0 \cdot \nu_e L_i \, ds,$$

the difference

$$\psi = \mathbf{v} - \pi_0^{\text{ME0}} \mathbf{v} = \mathbf{v} - \sum_{e \subset \partial E, i} \gamma_e^i \mathbf{v}_{0,e}^{M,i} = -a_0 \nabla \left(\phi_0 - \sum_{e \subset \partial E, i} \gamma_e^i \phi_{0,e}^{M,i} \right) \quad \text{in } E$$

is a potential field satisfying, for $F = \nabla \cdot \mathbf{v}_0$, the Neumann problem

$$\nabla \cdot \psi = F - \mathcal{P}_{W_H} F \quad \text{in } E, \quad \psi \cdot \nu_e = \mathbf{v}_0 \cdot \nu_e - \sum_i \gamma_e^i L_i \quad \text{on } e \subset \partial E.$$

We therefore have the standard energy estimate

$$\|\psi\|_{0,E} \leq C \left\{ \|F - \mathcal{P}_{W_H} F\|_{-1,E} + \sum_{e \subset \partial E} \left\| \mathbf{v}_0 \cdot \nu_e - \sum_i \gamma_e^i L_i \right\|_{-1/2,e} \right\},$$

and so, for $j = 1$ or, when $M = \text{ME1}$, $j = 1, 2$,

$$\|\mathbf{v}_0 - \pi_0^M \mathbf{v}_0\|_0 \leq C \{ \|F\|_{j-1} + \|\mathbf{v}_0\|_j \} H^j \leq C \|\mathbf{v}_0\|_j H^j,$$

since $\sum_i \gamma_e^i L_i$ is the best $L^2(e)$ constant or linear approximation of $\mathbf{v}_0 \cdot \nu_e$. \square

COROLLARY A.6. *Assuming (4.1), if Ω is a domain possessing the elliptic regularity property, and $M = \text{ME0}$ or ME1 , then there is some $\beta > 0$, independent of $\epsilon \leq H$, such that the following inf-sup condition holds:*

$$(A.15) \quad \sup_{\mathbf{v}_H \in \mathbf{V}_H^M} \frac{(w_H, \nabla \cdot \mathbf{v}_H)}{\|\mathbf{v}_H\|_0 + \|\nabla \cdot \mathbf{v}_H\|_0} \geq \beta \|w_H\|_0 \quad \forall w_H \in W_H.$$

Proof. The proof is fairly standard. For $w_H \in W_H$, we solve

$$\begin{aligned} \nabla \cdot \mathbf{v}_0 &= w_H && \text{in } \Omega, \\ \mathbf{v}_0 &= -a_0 \nabla \phi_0 && \text{in } \Omega, \\ \mathbf{v}_0 \cdot \nu &= 0 && \text{on } \partial\Omega, \end{aligned}$$

and conclude from elliptic regularity that

$$\|\mathbf{v}_0\|_1 \leq C \|w_H\|_0$$

for some constant C independent of ϵ . We take $\mathbf{v}_H = \pi_\epsilon^M \mathbf{v}_0 \in \mathbf{V}_H^M$, so $\nabla \cdot \mathbf{v}_H = \mathcal{P}_{W_H} \nabla \cdot \mathbf{v}_0 = w_H$ and, by Lemmas A.4 and A.5,

$$\begin{aligned} \|\mathbf{v}_H\|_0 &= \|\pi_\epsilon^M \mathbf{v}_0\|_0 \leq \|\pi_\epsilon^M \mathbf{v}_0 - \mathcal{A}_\epsilon \pi_0^M \mathbf{v}_0\|_0 + \|\mathcal{A}_\epsilon (\pi_0^M \mathbf{v}_0 - \mathbf{v}_0)\|_0 + \|\mathcal{A}_\epsilon \mathbf{v}_0\|_0 \\ &\leq C \left\{ \|\mathbf{v}_0\|_1 \left(\epsilon/H + \sqrt{\epsilon/H} \right) + \|\mathbf{v}_0\|_1 H + \|\mathbf{v}_0\|_0 \right\} \\ &\leq C_0 \|w_H\|_0, \end{aligned}$$

since $\|\mathcal{A}_\epsilon\|_{0,\infty}$ is bounded, where C_0 is independent of $\epsilon \leq H$. The result follows with $\beta = 1/(C_0 + 1)$. \square

A.3. Convergence results. In this section, we combine our results to prove the following theorem.

THEOREM A.7. *Assume that (4.1) holds, Ω is a domain possessing the elliptic regularity property, and $p_0 \in H^2(\Omega) \cap W^{1,\infty}(\Omega)$. Then for $M = \text{ME0}$ and $j = 1$ or ME1 and $j = 1, 2$,*

$$(A.16) \quad \|\mathbf{u}_\epsilon - \mathbf{u}_H^M\|_0 \leq C \{ (\epsilon + \epsilon/H + \sqrt{\epsilon/H}) \|\mathbf{u}_0\|_1 + H^j \|\mathbf{u}_0\|_j + \sqrt{\epsilon} \|\mathbf{u}_0\|_{0,\infty} \}$$

and, for $\epsilon \leq H$,

$$(A.17) \quad \|\mathcal{P}_{W_H} p_\epsilon - p_H\|_0 \leq C \|\mathbf{u}_\epsilon - \mathbf{u}_H^M\|_0.$$

Moreover, $\nabla \cdot \mathbf{u}_H^M = \mathcal{P}_{W_H} f$ and

$$(A.18) \quad \|\nabla \cdot (\mathbf{u}_\epsilon - \mathbf{u}_H^M)\|_0 \leq C\|f\|_1 H.$$

We have stated a convergence result for the projection of the pressure $\mathcal{P}_{W_H} p$ in (A.17), which implies only $\mathcal{O}(H)$ convergence of p_H to p itself. This can be improved by including the approximation (7.1)–(7.3) of the fixed source term f (see [7]).

Proof. Result (A.18) follows trivially from the definition of the finite element method (2.4).

Lemma A.1 gives us a convergence result if we can find a good approximation \mathbf{v}_ϵ of \mathbf{u}_ϵ in \mathbf{V}_H^M such that $\nabla \cdot \mathbf{v}_\epsilon = \mathcal{P}_{W_H} \nabla \cdot \mathbf{u}_\epsilon$. We claim that $\mathbf{v}_\epsilon = \pi_\epsilon^M \mathbf{u}_0 \in \mathbf{V}_H^M$ is a good choice. Note that Lemma A.3 gives the divergence condition. We combine Theorem 4.1 and Lemma A.4 to obtain that

$$(A.19) \quad \begin{aligned} \|\mathbf{u}_\epsilon - \mathbf{u}_H^M\|_0 &\leq C\|\mathbf{u}_\epsilon - \pi_\epsilon^M \mathbf{u}_0\|_0 \\ &\leq C\{\|\mathbf{u}_\epsilon - \mathcal{A}_\epsilon \mathbf{u}_0\|_0 + \|\mathcal{A}_\epsilon(\mathbf{u}_0 - \pi_0^M \mathbf{u}_0)\|_0 + \|\mathcal{A}_\epsilon \pi_0^M \mathbf{u}_0 - \pi_\epsilon^M \mathbf{u}_0\|_0\} \\ &\leq C\{(\epsilon + \epsilon/H + \sqrt{\epsilon/H})\|\mathbf{u}_0\|_1 + \sqrt{\epsilon}\|\mathbf{u}_0\|_{0,\infty} + \|\mathbf{u}_0 - \pi_0^M \mathbf{u}_0\|_0\}, \end{aligned}$$

since $\|\mathcal{A}_\epsilon\|_{0,\infty}$ is bounded. The proof of (A.16) then reduces to an analysis of the final term $\|\mathbf{u}_0 - \pi_0^M \mathbf{u}_0\|_0$, which is bounded by Lemma A.5.

Finally, the inf-sup condition Corollary A.6 and (A.3) give

$$\begin{aligned} \beta\|\mathcal{P}_{W_H} p_\epsilon - p_H\|_0 &\leq \sup_{\mathbf{v}_H \in \mathbf{V}_H^M} \frac{(\mathcal{P}_{W_H} p_\epsilon - p_H, \nabla \cdot \mathbf{v}_H)}{\|\mathbf{v}_H\|_0 + \|\nabla \cdot \mathbf{v}_H\|_0} \\ &= \sup_{\mathbf{v}_H \in \mathbf{V}_H^M} \frac{-(\alpha_\epsilon(\mathbf{u}_\epsilon - \mathbf{u}_H^M), \mathbf{v}_H)}{\|\mathbf{v}_H\|_0 + \|\nabla \cdot \mathbf{v}_H\|_0} \leq C\|\mathbf{u}_\epsilon - \mathbf{u}_H^M\|_0, \end{aligned}$$

which is (A.17). \square

The main part of the proof is the estimate of $\|\mathbf{u}_\epsilon - \mathbf{u}_H^M\|_0$ in (A.19), which consists of four simple parts:

- (1) quasi-optimality $\|\mathbf{u}_\epsilon - \pi_\epsilon^M \mathbf{u}_0\|_0$, Lemma A.1;
- (2) homogenization $\|\mathbf{u}_\epsilon - \mathcal{A}_\epsilon \mathbf{u}_0\|_0$, Theorem 4.1;
- (3) smooth approximation by the homogenized finite elements $\|\mathbf{u}_0 - \pi_0^M \mathbf{u}_0\|_0$, Lemma A.5; and
- (4) multiscale approximation $\|\mathcal{A}_\epsilon \pi_0^M \mathbf{u}_0 - \pi_\epsilon^M \mathbf{u}_0\|_0$, Lemma A.4.

Steps (1) and (2) are universal in this class of approximations, so one need only devise mixed multiscale finite elements that satisfy (3) and (4).

Interestingly, MD has good multiscale approximation properties (i.e., Lemma A.4 holds for MD), but it fails to approximate smooth functions with its corresponding homogenized finite elements.

The new HE0 elements are difficult to analyze rigorously, since the boundary condition (5.5) depends on ϵ . It is not clear how we should define the “homogenized” finite elements. What is clear is that, as $\epsilon \rightarrow 0$, $\mathcal{A}_\epsilon \rightarrow I$, the identity tensor (see (4.5) and (4.7)). Thus, in some sense, whatever homogenized elements we define, they should converge to the RT0 elements. If we take these as our homogenized elements, they satisfy the smooth function approximation requirement. However, we then need homogenization theory that treats the Neumann boundary condition to prove multiscale approximation properties. Such theory is not known to the author. But our analysis does suggest that the new homogenization-based elements should work well, and not suffer when the permeability is anisotropic.

A.4. A remark on convergence of nonmultiscale elements. The standard convergence estimate (2.12) for RT0 elements suggests that the error blows up as $\epsilon \rightarrow 0$, since

$$\|\mathbf{u} - \mathbf{u}_H^{\text{RT0}}\|_0 \leq C\|\mathbf{u}\|_1 H \sim CH/\epsilon \rightarrow \infty.$$

Under the assumption (4.1), this is in fact *not* the case: the error remains bounded as $\epsilon \rightarrow 0$. To see this, we use the optimality Lemma A.1, Theorem 4.1, and the standard approximation result for π^{RT0} to estimate

$$\begin{aligned} \|\mathbf{u} - \mathbf{u}_H^{\text{RT0}}\|_0 &\leq C\|\mathbf{u} - \pi^{\text{RT0}}\mathbf{u}_0\|_0 \\ &\leq C\{\|\mathbf{u} - \mathcal{A}_\epsilon\mathbf{u}_0\|_0 + \|(\mathcal{A}_\epsilon - I)\mathbf{u}_0\|_0 + \|\mathbf{u}_0 - \pi^{\text{RT0}}\mathbf{u}_0\|_0\} \\ &\leq C\{(\epsilon + H)\|\mathbf{u}_0\|_1 + \sqrt{\epsilon}\|\mathbf{u}_0\|_{0,\infty} + \|\mathbf{u}_0\|_0\} \leq C < \infty, \end{aligned}$$

independently of H and ϵ , since these are bounded. A similar bound can be derived for BDM1 elements.

REFERENCES

- [1] J. E. AARNES, *On the use of a mixed multiscale finite element method for greater flexibility and increased speed or improved accuracy in reservoir simulation*, Multiscale Model. Simul., 2 (2004), pp. 421–439.
- [2] J. E. AARNES, Y. EFENDIEV, AND L. JIANG, *Mixed multiscale finite element methods using limited global information*, Multiscale Model. Simul., 7 (2008), pp. 655–676.
- [3] J. E. AARNES, S. KROGSTAD, AND K.-A. LIE, *A hierarchical multiscale method for two-phase flow based upon mixed finite elements and nonuniform coarse grids*, Multiscale Model. Simul., 5 (2006), pp. 337–363.
- [4] T. ARBOGAST, *Numerical subgrid upscaling of two-phase flow in porous media*, in Numerical Treatment of Multiphase Flows in Porous Media, Lecture Notes in Phys. 552, Z. Chen, R. E. Ewing, and Z.-C. Shi, eds., Springer, Berlin, 2000, pp. 35–49.
- [5] T. ARBOGAST, *Implementation of a locally conservative numerical subgrid upscaling scheme for two-phase Darcy flow*, Comput. Geosci., 6 (2002), pp. 453–481.
- [6] T. ARBOGAST, *Analysis of a two-scale, locally conservative subgrid upscaling for elliptic problems*, SIAM J. Numer. Anal., 42 (2004), pp. 576–598.
- [7] T. ARBOGAST AND K. J. BOYD, *Subgrid upscaling and mixed multiscale finite elements*, SIAM J. Numer. Anal., 44 (2006), pp. 1150–1171.
- [8] T. ARBOGAST AND S. L. BRYANT, *Numerical subgrid upscaling for waterflood simulations*, in Proceedings of the 16th SPE Symposium on Reservoir Simulation, Houston, Texas, 2001.
- [9] T. ARBOGAST, S. E. MINKOFF, AND P. T. KEENAN, *An operator-based approach to upscaling the pressure equation*, in Computational Methods in Water Resources XII, Vol. 1: Computational Methods in Contamination and Remediation of Water Resources, V. N. Burganos, et al., eds., Computational Mechanics Publications, Southampton, UK, 1998, pp. 405–412.
- [10] T. ARBOGAST, G. PENCHEVA, M. F. WHEELER, AND I. YOTOV, *A multiscale mortar mixed finite element method*, Multiscale Model. Simul., 6 (2007), pp. 319–346.
- [11] I. BABUŠKA, G. CALOZ, AND J. E. OSBORN, *Special finite element methods for a class of second order elliptic problems with rough coefficients*, SIAM J. Numer. Anal., 31 (1994), pp. 945–981.
- [12] I. BABUŠKA AND R. LIPTON, *Optimal local approximation spaces for generalized finite element methods with application to multiscale problems*, Multiscale Model. Simul., 9 (2011), pp. 373–406.
- [13] I. BABUŠKA AND J. E. OSBORN, *Generalized finite element methods: Their performance and their relation to mixed methods*, SIAM J. Numer. Anal., 20 (1983), pp. 510–536.
- [14] A. BENSOUSSAN, J. L. LIONS, AND G. PAPANICOLAOU, *Asymptotic Analysis for Periodic Structure*, North-Holland, Amsterdam, 1978.
- [15] F. BREZZI, J. DOUGLAS, R. DURAN, JR., AND M. FORTIN, *Mixed finite elements for second order elliptic problems in three variables*, Numer. Math., 51 (1987), pp. 237–250.
- [16] F. BREZZI, J. DOUGLAS, JR., AND L. D. MARINI, *Two families of mixed elements for second order elliptic problems*, Numer. Math., 47 (1985), pp. 217–235.
- [17] F. BREZZI AND M. FORTIN, *Mixed and Hybrid Finite Element Methods*, Springer, New York, 1991.
- [18] Z. CHEN AND T. Y. HOU, *A mixed multiscale finite element method for elliptic problems with oscillating coefficients*, Math. Comp., 72 (2003), pp. 541–576.

- [19] M. A. CHRISTIE, *Tenth spe comparative solution project: A comparison of upscaling techniques*, SPE Reservoir Eval. Eng., 4 (2001), pp. 308–317.
- [20] P. G. CIARLET, *The Finite Element Method for Elliptic Problems*, North-Holland, Amsterdam, 1978.
- [21] W. E. AND B. ENQUIST, *The heterogeneous multiscale methods*, Commun. Math. Sci., 1 (2003), pp. 87–132.
- [22] Y. EFENDIEV AND T. Y. HOU, *Multiscale Finite Elements Methods*, Surv. Tutor. Appl. Math. Sci. 4, Springer, New York, 2009.
- [23] Y. R. EFENDIEV, T. Y. HOU, AND X.-H. WU, *Convergence of a nonconforming multiscale finite element method*, SIAM J. Numer. Anal., 37 (2000), pp. 888–910.
- [24] I. G. GRAHAM AND R. SCHEICHL, *Robust domain decomposition algorithms for multiscale PDEs*, Numer. Methods Partial Differential Equations, 23 (2007), pp. 859–878.
- [25] U. L. HETMANIUK AND R. B. LEHOUCQ, *A special finite element method based on component mode synthesis techniques*, ESAIM: Math. Modelling and Numer. Anal., 44 (2010), pp. 401–420.
- [26] U. Hornung, ed., *Homogenization and Porous Media*, Interdisciplinary Applied Mathematics Series 6, Springer, New York, 1997.
- [27] T. Y. HOU AND X. H. WU, *A multiscale finite element method for elliptic problems in composite materials and porous media*, J. Comput. Phys., 134 (1997), pp. 169–189.
- [28] T. Y. HOU, X.-H. WU, AND Z. CAI, *Convergence of a multiscale finite element method for elliptic problems with rapidly oscillating coefficients*, Math. Comp., 68 (1999), pp. 913–943.
- [29] T. J. R. HUGHES, *Multiscale phenomena: Green’s functions, the Dirichlet-to-Neumann formulation, sub-grid scale models, bubbles and the origins of stabilized methods*, Comput. Methods Appl. Mech. Engrg., 127 (1995), pp. 387–401.
- [30] T. J. R. HUGHES, G. R. FEIJÓO, L. MAZZEI, AND J.-B. QUINCY, *The variational multiscale method—a paradigm for computational mechanics*, Comput. Methods Appl. Mech. Engrg., 166 (1998), pp. 3–24.
- [31] T. J. R. HUGHES, A. A. OBERAI, AND L. MAZZEI, *Large eddy simulation of turbulent channel flows by the variational multiscale method*, Phys. Fluids, 13 (2001), pp. 1784–1799.
- [32] R. S. J. VAN LENT AND I. G. GRAHAM, *Energy minimizing coarse spaces for two-level Schwarz methods for multiscale PDEs*, Numer. Linear Algebra Appl., 16 (2009), pp. 775–799.
- [33] P. JENNY, S. H. LEE, AND H. A. TCHELEPI, *Adaptive multiscale finite-volume method for multiphase flow and transport in porous media*, Multiscale Model. Simul., 3 (2005), pp. 50–64.
- [34] P. JENNY, S. H. LEE, AND H. A. TCHELEPI, *Multi-scale finite-volume method for elliptic problems in subsurface flow simulation*, J. Comput. Phys., 187 (2003), pp. 47–67.
- [35] V. V. JIKOV, S. M. KOZLOV, AND O. A. OLEINIK, *Homogenization of Differential Operators and Integral Functions*, Springer, New York, 1994.
- [36] M. G. LARSON AND A. MÅLQVIST, *Adaptive variational multiscale methods based on a posteriori error estimation: Energy norm estimates for elliptic problems*, Comput. Methods Appl. Mech. Engrg., 196 (2007), pp. 2313–2324.
- [37] S. P. MAC LACHLAN AND J. D. MOULTON, *Multilevel upscaling through variational coarsening*, Water Resour. Res., 42 (2006), pp. 1–9.
- [38] J. NOLEN, G. PAPANICOLAOU, AND O. PIRONNEAU, *A framework for adaptive multiscale methods for elliptic problems*, Multiscale Model. Simul., 7 (2008), pp. 171–196.
- [39] J. M. NORDBOTTEN, *Adaptive variational multiscale methods for multiphase flow in porous media*, Multiscale Model. Simul., 7 (2009), pp. 1455–1473.
- [40] C. PECHSTEIN AND R. SCHEICHL, *Robust FETI solvers for multiscale elliptic PDEs*, in Mathematics in Industry—Scientific Computing in Electrical Engineering, Proceedings of the 6th Int. Conf. on Scientific Computing in Electrical Engineering, Springer, 2009.
- [41] M. PESZYNSKA, M. F. WHEELER, AND I. YOTOV, *Mortar upscaling for multiphase flow in porous media*, Comput. Geosci., 6 (2002), pp. 73–100.
- [42] R. A. RAVIART AND J. M. THOMAS, *A mixed finite element method for 2nd order elliptic problems*, in Mathematical Aspects of Finite Element Methods, Lecture Notes in Math. 606, I. Galligani and E. Magenes, eds., Springer, New York, 1977, pp. 292–315.
- [43] T. STROUBOULIS, K. COPPS, AND I. BABUŠKA, *The generalized finite element method*, Comput. Methods Appl. Mech. Engrg., 190 (2001), pp. 4081–4193.
- [44] L. TARTAR AND E. SANCHEZ-PALENCIA, *Incompressible fluid flow in a porous medium—convergence of the homogenization process*, in Non-homogeneous Media and Vibration Theory, Lecture Notes in Phys. 127, Springer, Berlin, 1980, pp. 368–377.
- [45] C. D. WHITE AND R. N. HORNE, *Computing absolute transmissibility in the presence of fine-scale heterogeneity*, in Proceedings of the Ninth SPE Symposium on Reservoir Simulation, 1987, pp. 209–220.